

# Testing the cosmological principle with the Pantheon+ sample and the region fitting method

J. P. Hu<sup>1</sup>, Y. Y. Wang<sup>2</sup>, J. Hu<sup>3</sup>, and F. Y. Wang<sup>1,4</sup>

<sup>1</sup> School of Astronomy and Space Science, Nanjing University, Nanjing 210093, China  
e-mail: fayinwang@nju.edu.cn

<sup>2</sup> Anton Pannekoek Institute for Astronomy, University of Amsterdam, Science Park 904, 1098 XH Amsterdam, Netherlands

<sup>3</sup> Institute of Astronomy and Information, Dali University, Dali 671003, China

<sup>4</sup> Key Laboratory of Modern Astronomy and Astrophysics (Nanjing University), Ministry of Education, Nanjing 210093, China

Received date; accepted date

## ABSTRACT

Cosmological principle is fundamental to the standard cosmological model. It assumes that the universe is homogeneous and isotropic on very large scales. As the basic assumption, it must stand the test of various observations. In this paper, we investigate the properties of Pantheon+ sample, including redshift distribution and position distribution, and give its constraint on the flat  $\Lambda$ CDM model:  $\Omega_m = 0.36 \pm 0.02$  and  $H_0 = 72.83 \pm 0.23 \text{ km s}^{-1} \text{ Mpc}^{-1}$ . Then, by using the region fitting (RF) method, we map the all-sky distribution of cosmological parameters ( $\Omega_m$  and  $H_0$ ) and find that the distribution significantly deviates from isotropy. There exists a local matter underdensity region toward  $(313.4^{+19.6}_{-18.2}, -16.8^{+11.1}_{-10.7})$  and a preferred direction of the cosmic anisotropy  $(308.4^{+47.6}_{-48.7}, -18.2^{+21.1}_{-28.8})$  in galactic coordinates. Similar directions may imply that local matter density might be responsible for the anisotropy of the accelerated expansion of the universe. Results of statistical isotropy analyses including Isotropy and Isotropy with real-data positions (RP) show high confidence levels. For the local matter underdensity, the statistical significances are  $2.78\sigma$  (Isotropy) and  $2.34\sigma$  (Isotropy (RP)). For the cosmic anisotropy, the statistical significances are  $3.96\sigma$  (Isotropy) and  $3.15\sigma$  (Isotropy (RP)). The comparison of these two kinds of statistical isotropy analyses suggests that inhomogeneous spatial distribution of real sample can increase the deviation from isotropy. The similar results and findings are also found from reanalyses of the low-redshift sample (lp+) and the lower screening angle ( $\theta_{\max} = 60^\circ$ ), but with a slight decrease in statistical significance. Overall, our results provide clear indications for a possible cosmic anisotropy. This possibility must be taken seriously. Further testing is needed to better understand this signal.

**Key words.** cosmology: theory – cosmological parameters – supernovae: general

## 1. Introduction

The  $\Lambda$ CDM is generally accepted as the standard cosmological model, which is consistent with the most astronomical observations (Scolnic et al. 2018; Abbott et al. 2019; Khadka & Ratra 2020; Brout et al. 2022; Cao & Ratra 2022; Dainotti et al. 2022b; Jia et al. 2022; Liu et al. 2022a; Porredon et al. 2022; Wang et al. 2022; de Cruz Pérez et al. 2023; Khadka et al. 2023; Li et al. 2023b). It is based on the fundamental assumption of the cosmological principle, namely the Universe is statistically isotropic and homogeneous on sufficiently large scales. Despite its many successes, there has been also several analyses of observations which indicate that the Universe may be inhomogeneous and anisotropic, for instance the fine-structure constant, (Webb et al. 2011; King et al. 2012; Li & Lin 2017; Milaković et al. 2022), the direct measurement of Hubble parameter (Bonvin et al. 2006; Koksang 2021), the cosmic microwave background (CMB) (Bennett et al. 2003; Tegmark et al. 2003; Bielewicz et al. 2004; Bennett et al. 2011; Gruppuso et al. 2011; Ghosh & Jain 2020; Planck Collaboration et al. 2020c), the anisotropic dark energy (Koivisto & Mota 2008; Mariano & Perivolaropoulos 2012; Bayron Orjuela-Quintana et al. 2020; Motoa-Manzano et al. 2021), the large dipole of radio source counts (Rubart et al. 2014; Colin et al. 2017; Rameez et al. 2018; Singal 2019, 2023), quasar dipole (Hutsemékers et al. 2005; Pel-

grims & Hutsemékers 2016; Tiwari & Jain 2019; Hu et al. 2020; Secrest et al. 2021; Zhao & Xia 2021a,b), the anisotropic Hubble constant (Luongo et al. 2022; McConville & Colgáin 2023) and the type Ia supernovae (SNe Ia) dipole (Colin et al. 2011; Yang et al. 2014; Javanmardi et al. 2015; Sun & Wang 2018; Wang & Wang 2018; Tang et al. 2023), local matter underdensity (Kazantzidis & Perivolaropoulos 2020). These analyses hint that the Universe may have a local void and a preferred expanding direction. In addition, it is assumed that the  $\Lambda$ CDM model also triggers a serious Hubble constant discrepancy between the *Planck* CMB (Planck Collaboration et al. 2020b) and the local distance ladder (Riess et al. 2019, 2022). This is known as the Hubble tension, and its statistical significance has reached  $5.0\sigma$ . Such a high confidence could not be explained by systematic alone, and might imply new physics beyond the  $\Lambda$ CDM model. Focusing on this issue, there has been intense discussion and a lot of theoretical explanations have been proposed. We refer the readers to some review articles (Di Valentino et al. 2021; Shah et al. 2021; Abdalla et al. 2022; Perivolaropoulos & Skara 2022; Hu & Wang 2023; Kumar Aluri et al. 2023; Pavel et al. 2023; Riess & Breuval 2023; Vagnozzi 2023) for more detail information about the cosmological anomalies and tension.

It is worth noting that some researches claim considering a void model can successfully explain away the cosmic dipole

and the Hubble tension (Böhringer et al. 2020; Haslbauer et al. 2020; Luković et al. 2020; Camarena et al. 2022; Cai et al. 2022). Haslbauer et al. (2020) showed for the first time that the KBC void (Keenan et al. 2013) could naturally resolve the Hubble tension in Milgromian dynamics. By computing the Hubble constant in an inhomogeneous universe and adopting model selection via both the Bayes factor and the Akaike information criterion, Camarena et al. (2022) found that the Lambda Lemaître-Tolman-Bondi (ALTB) model is favored with respect to the  $\Lambda$ CDM model at low-redshift range ( $0.023 < z < 0.15$ ), and this can be used to explain away the Hubble tension. After that, Cai et al. (2022) proposed that a gigaparsec scale void can reconcile the CMB and quasar dipolar tension. If considering a large and thick void, their setup can also ease the Hubble tension. At the same time, there are also some findings which could be explained by a local void model. For example, inspired by the H0LICOW results (Millon et al. 2020; Wong et al. 2020), Hu & Wang (2022b) reported a late-time transition of  $H_0$  i.e.,  $H_0$  changes from being consistent with the CMB result to being consistent with the distance ladder one from an early to late cosmic time that can be explicated by the local void. The late-time transition of  $H_0$  was found from the observational Hubble parameter  $H(z)$  data combining the Gaussian process (GP) method (Pedregosa et al. 2011), and can be used to effectively relieve the Hubble tension (a mitigation level of around 70 percent). In addition, a similar  $H_0$  descending behavior has been also discovered by utilizing various observations (such as SNe Ia,  $H(z)$ , BAOs and megamasers) and their combinations (Krishnan et al. 2020, 2021b; Dainotti et al. 2022a; Ó Colgáin et al. 2022; Horstmann et al. 2022; Colgáin et al. 2022; Jia et al. 2023; Malekjani et al. 2023). Of course, there are also some opposing voices, who believe that the void model alone cannot solve the Hubble tension (Kenworthy et al. 2019; Cai et al. 2021; Castello et al. 2022). Therefore, further research on this controversial topic is very necessary and meaningful. So far, there has been no research using the Pantheon+ sample to simultaneously map matter density ( $\Omega_m$ ) distribution and the Hubble expansion ( $H_0$ ) distribution to test the cosmological principle.

In this paper, we test the cosmological principle by the region fitting (RF) method with the latest Pantheon+ sample. Different from the previous work (Krishnan et al. 2021a, 2022; McConville & Colgáin 2023), we improve our research methodology and make the necessary statistical analyses. Usually, considering the simple flat  $\Lambda$ CDM model,  $\Omega_m$  and  $H_0$  are considered to be negatively correlated. Therefore, for the convenience of analysis, one parameter is usually fixed. For example, some recent works fix  $\Omega_m$  to 0.30 and regard  $H_0$  as a free parameter (Krishnan et al. 2021a, 2022; McConville & Colgáin 2023). In our fitting calculation process, all cosmological parameter ( $\Omega_m$  and  $H_0$ ) are free to investigate the local properties of our Universe. We would like to plot the all-sky distributions of  $\Omega_m$  and  $H_0$  to find out the local matter underdensity region and the preferred direction of expansion (cosmic anisotropy), respectively. The influence of redshift and screening angle  $\theta_{\max}$  on the final results is also considered. We find out the suitable angle of RF method for the Pantheon+ sample. Then we make a detailed discussion combining the local void (Enqvist 2008; Garcia-Bellido & Haugbølle 2008; Keenan et al. 2013; Wang & Dai 2013; Hwang et al. 2016; Hamaus et al. 2022; Shim et al. 2023), cosmic anisotropy (Sun & Wang 2019; Akarsu et al. 2020; Migkas et al. 2020, 2021; Akarsu et al. 2022; Horstmann et al. 2022; Rahman et al. 2022; Akarsu et al. 2023; Dhawan et al. 2023; Ebrahimian et al. 2023) and Hubble tension (Chen 2019; Riess et al. 2019; Verde et al. 2019; Planck Collaboration et al. 2020b; Riess 2020; Riess et al.

2022; Capozziello et al. 2023). Finally, our results are compared with previous similar researches (Antoniou & Perivolaropoulos 2010; Cai & Tuo 2012; Kalus et al. 2013; Wang & Wang 2014; Yang et al. 2014; Chang & Lin 2015; Lin et al. 2016b; Chang & Zhou 2019; Hu et al. 2020; Luongo et al. 2022; McConville & Colgáin 2023) and other observations, including the CMB dipole (Planck Collaboration et al. 2016, 2020a), dark flow (Abdalla et al. 2022), bulk flow (Turnbull et al. 2012; Feix et al. 2017; Watkins et al. 2023) and galaxy cluster (Migkas et al. 2021).

The outline of this paper is as follows. In Section 2, compared with the Pantheon sample, we give a detailed description of the Pantheon+ sample, including redshift distribution, location distribution and corresponding density contour. Section 3 briefly introduces the region fitting (RF) method which is used to map the all-sky distribution of cosmological parameters. In Section 4, we present the results from the whole and low-redshift Pantheon+ sample ( $z < 0.30$ , lp+) and discuss the impact of RF method with different screening angles  $\theta_{\max}$  on the final results from the Pantheon+ sample. The corresponding investigation and discussion are arranged in section 5. Finally, conclusions and perspectives are presented in the last Section.

## 2. Pantheon+ sample

Pantheon+, as the latest sample of SNe Ia, consists of 1701 SNe Ia light curves observed from 1550 distinct SNe and covers redshift range from 0.001 to 2.26 (Brout et al. 2022; Scolnic et al. 2022). The redshift distribution of the Pantheon (Scolnic et al. 2018) and Pantheon+ samples are shown in Fig. 1. From the redshift distribution of these two samples, it is not difficult to find that there are two main differences between the new sample and the Pantheon sample. One is that the SN number has increased significantly at low redshift. There are more than 700 additional SNe in the range of  $z < 0.8$ , of which more than 500 SNe originated from  $z < 0.08$ . This is mainly because the new sample adds five large samples, including the Foundation Supernova Survey (Foundation; Foley et al. 2018), the Swift Optical/Ultraviolet Supernova Archive (SOUSA; Brown et al. 2014), the Lick Observatory Supernova Search (LOSS1; Ganeshalingam et al. 2010), the second sample from LOSS (LOSS2; Stahl et al. 2019) and the Dark Energy Survey 3 years (DES; Brout et al. 2019; Smith et al. 2020), all of which are low-redshift surveys except DES. The other difference is that there exists a significant deletion in Pantheon+ statistic between  $0.8 < z < 1.0$ . The reason is that Scolnic et al. (2022) does not use SNe from the Supernova Legacy Survey (SNLS) at  $z > 0.8$  considering sensitivity to the  $U$  band in model training (56 SNe in total).

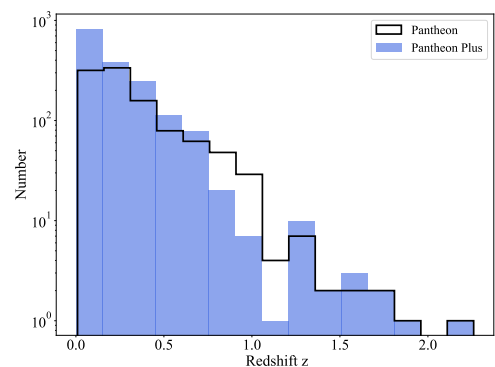


**Fig. 1.** The redshift distribution of the Pantheon and Pantheon+ samples.

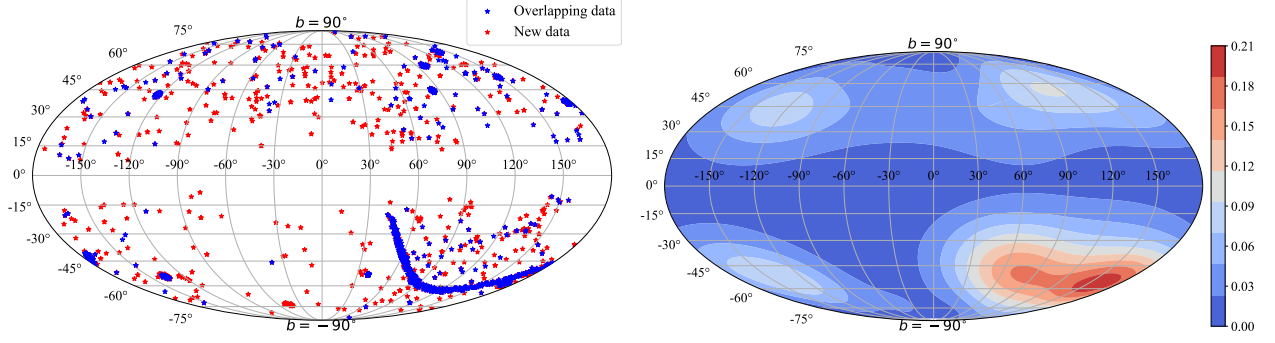


**Fig. 2.** Distribution and corresponding density contour in the galactic coordinate system. Left panel shows the SNe distribution of the Pantheon sample. Red and blue points represent the new added SNe and the SNe where the Pantheon sample and the Pan sample overlap, respectively. Right panel shows the corresponding density contour.

Figure 2 shows the distribution (left panel) and corresponding density (right panel) of the Pantheon+ sample in the sky of the galactic coordinate system. Some previous work has pointed out that the Pantheon SNe Ia are not uniformly distributed in the sky, half of them are located in the galactic south-east. A part of SNe are very concentrated, forming a belt-like structure, i.e. SDSS sample (Zhao et al. 2019). At the same time, Zhao et al. (2019) also investigated the effect of the inhomogeneous distribution of the Pantheon sample on the cosmic anisotropy and found that the belt-like structure plays the most important role in the Pantheon sample. In the left panel, to highlight the difference between these two samples, we mark the newly added SNe Ia in red. From the distribution of Pantheon+ sample, we find that the distribution of the new data is still uneven across the sky. There are only fewer observations near  $(l, b) \sim (300^\circ, -30^\circ)$ . Its incomplete sky coverage is primarily due to the fact that the Pantheon+ sample consists of different subsamples, following multiple measurement strategies. In order to make it easier to comprehend this focus, we also plot the density distribution of the Pantheon+ sample utilizing the `plt.contour()` function<sup>1</sup>, as shown in the right panel of Fig. 2. Color-coded values represent sample fraction per unit area. From the density distribution, we can more intuitively feel the inhomogeneity of sample distribution. As can be seen, the belt-like part of the Pantheon+ sample still plays the most important role as in the case of the Pantheon sample while the maximum density value change from 0.24 to 0.21 (Hu et al. 2020). This means that the Pantheon+ sample is more uniform than the Pantheon sample. The newly added SNe Ia effectively weaken the dominance of the belt structure in the distribution. The Pantheon+ sample that is relatively uniform and rich in low redshift is very suitable for analyzing the local property of the Universe (Andrade et al. 2018; Luongo et al. 2022; Kalbounh et al. 2023). Here, we use the hemisphere method combined with the Pantheon+ sample to describe the all-sky distribution of cosmological parameters to study the local structure of the Universe, and the detailed analysis process is shown in the next section.

### 3. Region fitting method

Hemisphere comparison (HC) method which proposed by Schwarz & Weinhorst (2007) has been widely used to the investigation of the cosmic anisotropy, such as the anisotropy of cosmic expansion (Deng & Wei 2018a; Zhao & Xia 2022), the

acceleration scale of modified Newtonian dynamics (Zhou et al. 2017; Chang et al. 2018; Chang & Zhou 2019) and the temperature anisotropy of the CMB (Hansen et al. 2004; Bennett et al. 2013; Ghosh et al. 2016; Ferreira & Quartin 2021). Our used region fitting (RF) method, is similar to it. Here, we make a detailed introduction to this method. Its goal is to map the all-sky distribution of the cosmological parameters. The most important step is to generate random directions  $\hat{D}(l, b)$  for picking out SNe data located in specific regions to construct subdatasets, where  $l \in (0^\circ, 360^\circ)$  and  $b \in (-90^\circ, 90^\circ)$  are the longitude and latitude in the galactic coordinate system, respectively. The specific region is given by condition  $(\theta < \theta_{\max})$ .  $\theta$  is the angle between the random direction  $\hat{D}(l, b)$  and the SN position. Here we refer to  $\theta_{\max}$  as the screening angle which used to obtain regions of different sizes, and the value range is  $(0^\circ, 180^\circ)$ . The remaining steps can be divided into three parts, which will be presented in subsections.

#### 3.1. Fitting parameters

According to subdatasets obtained in the previous step, the corresponding best fits of the cosmological parameters are obtained by minimizing value of  $\chi^2$ ,

$$\chi^2 = \Delta\mu \mathbf{C}_{\text{stat+sys}}^{-1} \Delta\mu^T, \quad (1)$$

where  $\Delta\mu$  is the difference between the observational distance modulus  $\mu_{\text{obs}}$  and the theoretical distance modulus  $\mu_{\text{th}}$ :

$$\Delta\mu = \mu_{\text{obs}}(z_i) - \mu_{\text{th}}(\Omega_m, H_0, z_i). \quad (2)$$

For the flat  $\Lambda$ CDM model, the corresponding form of  $\mu_{\text{th}}$  can be written as

$$\mu_{\text{th}}(\Omega_m, H_0, z_i) = m - M = 5 \log_{10} \frac{d_L(\Omega_m, H_0, z_i)}{\text{Mpc}} + 25, \quad (3)$$

here,  $z_i$  is the peculiar-velocity corrected CMB-frame redshift of each SN (Carr et al. 2022),  $m$  is the apparent magnitude of the source,  $M$  is the absolute magnitude, and  $d_L$  is the luminosity distance expressed in Mpc, defined in following equation

$$d_L = \frac{c(1+z)}{H_0} \int_0^z \frac{dz'}{\sqrt{\Omega_m(1+z')^3 + (1-\Omega_m)}}, \quad (4)$$

where  $c$  is the speed of light.

The statistical ( $\mathbf{C}_{\text{stat}}$ ) and systematic covariance matrices ( $\mathbf{C}_{\text{sys}}$ ) are combined and adopted to constrain the cosmological parameters:

$$\mathbf{C}_{\text{stat+sys}} = \mathbf{C}_{\text{stat}} + \mathbf{C}_{\text{sys}}. \quad (5)$$

<sup>1</sup> [https://matplotlib.org/stable/gallery/images\\_contours\\_and\\_fields/irregulardatagrid.html](https://matplotlib.org/stable/gallery/images_contours_and_fields/irregulardatagrid.html)

It is noted that our used datasets,  $\mu_{\text{obs}}$  and  $\mathbf{C}_{\text{stat+sys}}$  are provided by Brout et al. (2022), can be obtained from website<sup>2</sup>.  $\mathbf{C}_{\text{stat+sys}}$  includes all the covariance between SNe (and also Cepheid host covariance) due to systematic uncertainties (Brout et al. 2022).  $\mathbf{C}_{\text{stat}}$  mainly includes the full distance error and measurement noise.  $\mathbf{C}_{\text{sys}}$  can manifest in three key places in the analysis: (1) from changing aspects affecting the light-curve fitting, (2) from changing redshifts that propagate to changes in distance modulus relative to a cosmological model, and (3) from changes in the simulations used for bias corrections (Brout et al. 2022). More detailed information about the covariance matrices can be found from Sec. 2.2 of Brout et al. (2022). Unlike the previous analyses (Betoule et al. 2014; Colin et al. 2019), we did not introduce an intrinsic scatter. So in the fitting process, there are only two free parameters ( $\Omega_m$  and  $H_0$ ), which makes them strongly correlated. For the different subdatasets,  $\Omega_m$  and  $H_0$  are fitted simultaneously. Our used  $\mathbf{C}_{\text{stat+sys}}$  are obtained by cropping the total covariance matrix according to the SNe Ia subsample. In this paper, the minimization is performed employing a Bayesian Monte Carlo Markov Chain (MCMC) (Foreman-Mackey et al. 2013) with the *emcee* package<sup>3</sup>. All the fittings in this paper are obtained adopting this python package. The MCMC samples are plotted by utilizing the *getdist* package (Lewis 2019).

### 3.2. All-sky distribution

During the calculation, we repeated 5000 random directions  $\hat{D}(l, b)$ , i.e. 5000 sets of best fitting results ( $\Omega_m$  and  $H_0$ ). Based on the fitting results, the all-sky distributions of  $\Omega_m$  and  $H_0$  are mapped, respectively. From the distribution of  $\Omega_m$  and  $H_0$ , we can obtain the information of local matter underdensity and cosmic anisotropy, respectively. In order to describe the degree of deviation from the cosmological principle, we define a parameter  $D_{\text{max}}(\sigma)$  whose form is as follow

$$D_{\text{max}}(\sigma) = \frac{P_{\text{max}} - P_{\text{min}}}{\sqrt{\sigma_{P_{\text{max}}}^2 + \sigma_{P_{\text{min}}}^2}}. \quad (6)$$

Here,  $P_{\text{min}}$  and  $P_{\text{max}}$  are the minimum value and the maximum value of the best fitting results, respectively.  $\sigma_{P_{\text{min}}}$  and  $\sigma_{P_{\text{max}}}$  are the corresponding  $1\sigma$  error. The local matter underdensity direction and the preferred direction of cosmic anisotropy are marked by the corresponding location of the lowest  $\Omega_m$  and the largest  $H_0$ . The corresponding  $1\sigma$  regions are plotted in term of the values of  $P_0$  which is calculated from

$$1.00(\sigma) \geq \frac{P_0 - P_{\text{fit}}}{\sqrt{\sigma_{P_0}^2 + \sigma_{P_{\text{fit}}}^2}}, \quad (7)$$

where  $P_{\text{fit}}$ , representing the lowest  $\Omega_m$  constraint or the largest  $H_0$  constraint, is used to find the  $1\sigma$  range of the local matter underdensity direction or the preferred direction.  $\sigma_{P_{\text{fit}}}$  represents the corresponding error.  $P_0$  represents the constraints which consistent with  $P_{\text{fit}}$  within  $1\sigma$  error, and  $\sigma_{P_0}$  are the corresponding  $1\sigma$  values. Note,  $P_0$  and  $\sigma_{P_0}$  are filtered from the total  $\Omega_m/H_0$  fitting results depending on Eq. 7. Here,  $P_0$  and  $P_{\text{fit}}$  are completely independent, obtained using different SNe subsamples.

### 3.3. Statistical analyses

In order to examine whether the discrepancy degree of the cosmological parameters from the Pantheon+ sample is consistent

<sup>2</sup> <https://github.com/PantheonPlusSH0ES/DataRelease>

<sup>3</sup> <https://emcee.readthedocs.io/en/stable/>

with statistical isotropy, we plan to make statistical isotropic analyses. To achieve this, we spread the original data set evenly across the sky. After that, we can obtain the  $D_{\text{max}}$  for the isotropic data-set. Meanwhile, an additional isotropic analysis is also considered. We preserve the spatial inhomogeneity of real sample and then randomly distribute the real data-set, i.e. randomly redistribute only the distance moduli & redshift combination to real-data positions (RP). Given the limitations of computing time, we repeated it 500 times that have acceptable statistics. For convenience, we refer these two approach as Isotropy analysis and Isotropy(RP) analysis.

## 4. Results

We first give the best fitting results in the flat  $\Lambda$ CDM model employing the full Pantheon+ sample,  $\Omega_m = 0.36 \pm 0.02$  and  $H_0 = 72.83 \pm 0.23 \text{ km s}^{-1} \text{ Mpc}^{-1}$ . The results are in line with the previous research (Brout et al. 2022), except that the  $1\sigma$  error of  $H_0$  reduced. The main reason is that we utilized the standardized distance modulus ( $\mu_{\text{obs}}$ ; Tripp 1998) where fiducial  $M$  has been determined from SH0ES 2021 Cepheid host distances (Riess et al. 2022).

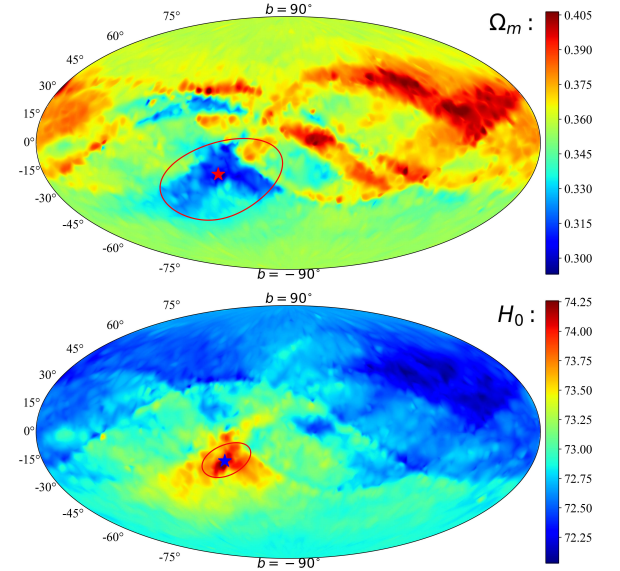


**Fig. 3.** All-sky distribution of the cosmological parameters utilizing the Pantheon+ sample combined with the  $90^\circ$  RF method. The left and the right panel show the results of  $\Omega_m$  and  $H_0$ , respectively. The corresponding values of  $D_{\text{max}}(\sigma)$  are  $3.29\sigma$  and  $4.48\sigma$ , respectively. The star marks the directions of the lowest  $\Omega_m$  (left panel) and the largest  $H_0$  (right panel), and the red circle outlines the corresponding  $1\sigma$  areas. The directions and  $1\sigma$  areas are parameterized as  $\Omega_{m,\text{min}} (308.4^{+47.6}_{-48.7}, -18.2^{+21.1}_{-28.8})$  and  $H_{0,\text{max}} (313.4^{+19.6}_{-18.2}, -16.8^{+11.1}_{-10.7})$ .

After that, using the RF method with a screening angle  $\theta_{\text{max}} = 90^\circ$ , we map the all-sky distribution of  $\Omega_m$  and  $H_0$  and draw the  $1\sigma$  regions of local matter underdensity and cosmic anisotropy, as shown in the upper panel and lower panel of Fig. 3, respectively. In Fig. 3, the range of  $\Omega_m$  and  $H_0$  are (0.29, 0.41) and (72.03, 74.26) respectively. The corresponding differences are  $\Delta\Omega_m = 0.12$  and  $\Delta H_0 = 2.23 \text{ km s}^{-1} \text{ Mpc}^{-1}$ . The values of  $D_{\text{max}}$  to  $\Omega_m$  and  $H_0$  are  $D_{\text{max},\Omega_m} = 3.29\sigma$  and  $D_{\text{max},H_0} = 4.48\sigma$ , respectively. In the upper panel of Fig. 3, the minimum constraint of  $\Omega_m$  is  $0.29^{+0.03}_{-0.02}$  ( $1\sigma$ ) and the corresponding constraint fo  $H_0$  is  $74.11^{+0.40}_{-0.40} \text{ km s}^{-1} \text{ Mpc}^{-1}$ . The direction and corresponding  $1\sigma$  range that can be adopted to describe the local matter



underdensity are

$$(l, b) = (308.4^{+47.6}_{-48.7}, -18.2^{+21.1}_{-28.8}). \quad (8)$$

The lower panel of Fig. 3 shows the corresponding all-sky distribution of the Hubble expansion. The maximum constraint of  $H_0$  is  $H_{0,\max} = 74.26 \pm 0.39 \text{ km s}^{-1} \text{ Mpc}^{-1}$ , and the corresponding constraint of  $\Omega_m$  is  $0.30^{+0.03}_{-0.03}$ . Its confidence contours are shown in Fig. 4, marked with blue lines. The preferred direction of cosmic anisotropy and corresponding  $1\sigma$  range are

$$(l, b) = (313.4^{+19.6}_{-18.2}, -16.8^{+11.1}_{-10.7}). \quad (9)$$

In Fig. 4, we also give the best fitting results of opposite direction, i.e.,  $H_{0,\min} = 72.14^{+0.27}_{-0.27} \text{ km s}^{-1} \text{ Mpc}^{-1}$  and  $\Omega_m = 0.40^{+0.02}_{-0.02}$  which marked with red lines.

The statistical isotropic results as shown in Fig. 5 can be well described by Gaussian functions. For the Isotropy analysis, the statistical significance ( $\alpha$ ) of the real data are  $2.78\sigma$  for  $\Omega_m$  anisotropy (upper, purple panel) and  $3.96\sigma$  for  $H_0$  anisotropy (upper, blue panel). The statistical significance ( $\beta$ ) of the real data given by the Isotropy (RP) analysis are  $2.34\sigma$  for  $\Omega_m$  anisotropy (lower, purple panel) and  $3.15\sigma$  for  $H_0$  anisotropy (lower, blue panel).

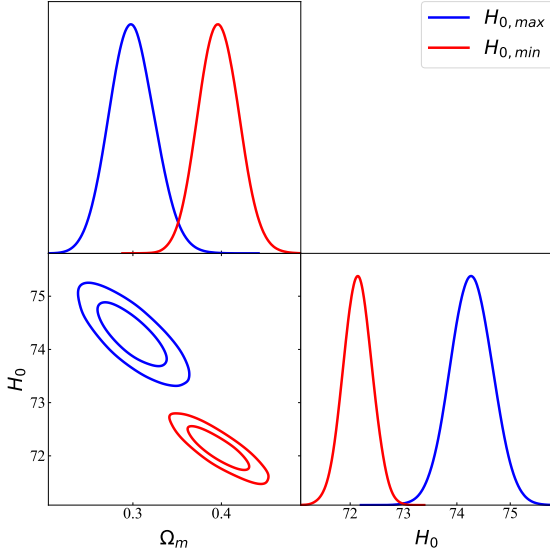


**Fig. 4.** Confidence contours ( $1\sigma$  and  $2\sigma$ ) and marginalized likelihood distributions for the parameters space ( $\Omega_m$  and  $H_0$ ) in the spatially flat  $\Lambda$ CDM model from the SNe Ia subsamples which corresponds to  $H_{0,\min}$  (red line) and  $H_{0,\max}$  (blue line). The best fitting results of preferred direction are  $H_{0,\max} = 74.26^{+0.40}_{-0.39} \text{ km s}^{-1} \text{ Mpc}^{-1}$ ,  $\Omega_m = 0.30^{+0.03}_{-0.03}$  (blue line). The best fitting results of opposite direction are  $H_{0,\min} = 72.14^{+0.27}_{-0.27} \text{ km s}^{-1} \text{ Mpc}^{-1}$  and  $\Omega_m = 0.40^{+0.02}_{-0.02}$  (red line).

#### 4.1. Reanalyses at low redshift

Recently, Hu & Wang (2022b) report a late-time transition of  $H_0$ , i.e.  $H_0$  changes from a low value to a high one from early to late cosmic time, by combining the GP method and  $H(z)$  data. The  $H_0$  transition occurs at  $z \sim 0.49$ . From other observations, a similar descending behavior of  $H_0$  has been found adopting other methods, see (Hu & Wang 2023) for a review of  $H_0$  descending trend. Around  $z \sim 0.40$ ,  $H_0$  starts to decrease (Jia et al. 2023). Both the transition behavior and the descending trend of  $H_0$  can effectively alleviate the Hubble tension. A few months ago, Kelly

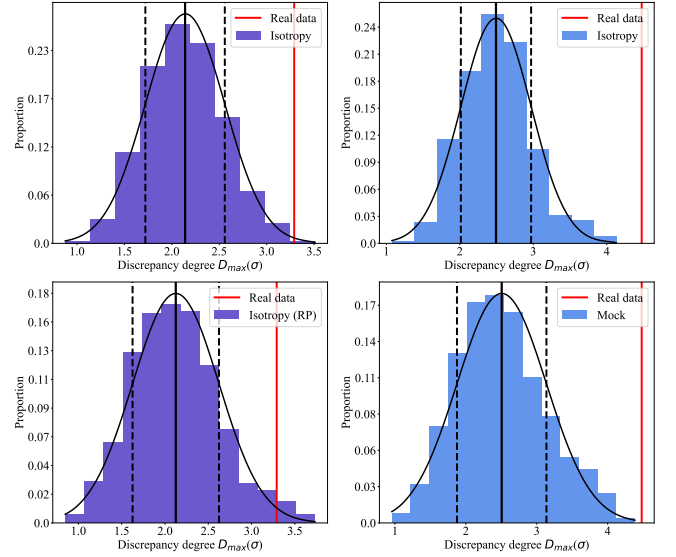


**Fig. 5.** Distribution of the discrepancy degree  $D_{\max}$  in 500 simulated isotropic datasets. The upper two panels show the results of statistical isotropic analyses (Isotropy). The lower two panels show the results of statistical isotropic analyses that preserve the spatial inhomogeneity of real data (Isotropy (RP)). The purple and blue represent the statistical results of  $\Omega_m$  and  $H_0$ . The black curve is the best fitting to the Gaussian function. The solid black and vertical dashed lines are commensurate with the mean and the standard deviation, respectively. The red lines represent the discrepancy degree from the real data. For the Isotropy analyses, the statistical significance of the real data are  $2.78\sigma$  for  $\Omega_m$  anisotropy;  $3.96\sigma$  for  $H_0$  anisotropy. For the Isotropy (RP) analyses, the statistical significance of the real data are  $2.34\sigma$  and  $3.15\sigma$  for  $\Omega_m$  and  $H_0$  anisotropy, respectively.

et al. (2023) gave new  $H_0$  measurements from the gravitationally lensed SNe Ia Refsdal (Refsdal 1964). The redshifts of the lens and the source are 0.54 and 1.49 (Kelly et al. 2015), respectively. Utilizing eight cluster lens models, they inferred  $H_0 = 64.80^{+4.40}_{-4.30} \text{ km s}^{-1} \text{ Mpc}^{-1}$ . Then Using the two models most consistent with observations, they found  $H_0 = 66.60^{+4.10}_{-3.30} \text{ km s}^{-1} \text{ Mpc}^{-1}$ . Marking the values of lensing redshift and  $H_0$  on Fig. 3 in Hu & Wang (2022b) and Fig. 4 in Jia et al. (2023), we can find that these results are in good agreement with the evolutionary behaviors of  $H_0$ . Motivated by the  $H_0$  special behaviors in the late-time universe, we plan to construct a low-redshift subsample based on the Pantheon+ sample to make a reanalyses. According to the previous researches (Hu & Wang 2022b; Jia et al. 2023), and considering the need for a sufficient sample size, we decided to select 1218 SNe with redshift less than 0.30 in the Pantheon+ sample to construct sub-sample (named the lp+ sample). Detailed steps and results are as follows.

At first, we give the cosmological constraint in the flat  $\Lambda$ CDM model using the lp+ sample, i.e.  $\Omega_m = 0.44 \pm 0.04$  and  $H_0 = 72.43 \pm 0.30 \text{ km s}^{-1} \text{ Mpc}^{-1}$ , which is consistent with the results from the full Pantheon+ sample and from Fig. 16 in (Brout et al. 2022). For ease of comparison, we give the constraint results of the Pantheon+ and lp+ samples in Fig. 6. Then we reproduce the previous analyses. All-sky distribution, the cosmological constraints and the isotropic statistic results are shown in Figs. 7, 8 and 9 respectively. From Fig. 7, it is easy to get the ranges of constraints,  $\Omega_m$  (0.25, 0.58) and  $H_0$  (71.43, 74.11)  $\text{km s}^{-1} \text{ Mpc}^{-1}$ . The corresponding differences are  $\Delta\Omega_m = 0.33$  and  $\Delta H_0 = 2.68 \text{ km s}^{-1} \text{ Mpc}^{-1}$ . By calculation, we get  $D_{\max, \Omega_m} = 4.17\sigma$  and  $D_{\max, H_0} = 4.49\sigma$ . The directions and  $1\sigma$  regions of

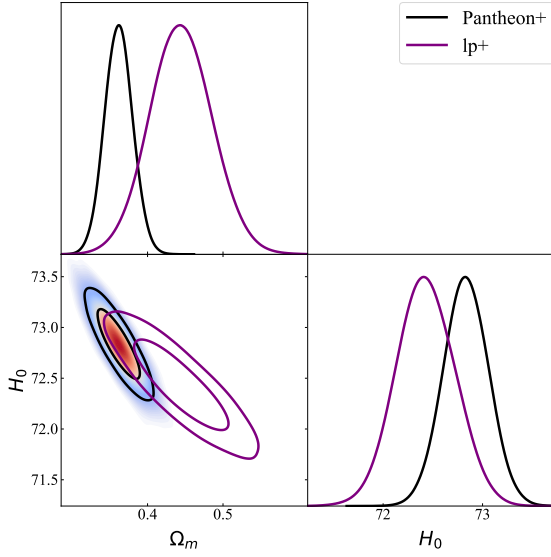


**Fig. 6.** Confidence contours ( $1\sigma$  and  $2\sigma$ ) and marginalized likelihood distributions for the parameters space ( $\Omega_m$  and  $H_0$ ) in the spatially flat  $\Lambda$ CDM model from the Pantheon+ sample and the lp+ sample. For the former, the best fits are  $\Omega_m = 0.36 \pm 0.02$  and  $H_0 = 72.83 \pm 0.23 \text{ km s}^{-1} \text{ Mpc}^{-1}$  (black line). For the latter, the best fits are  $\Omega_m = 0.44 \pm 0.04$  and  $H_0 = 72.43 \pm 0.30 \text{ km s}^{-1} \text{ Mpc}^{-1}$  (purple line).

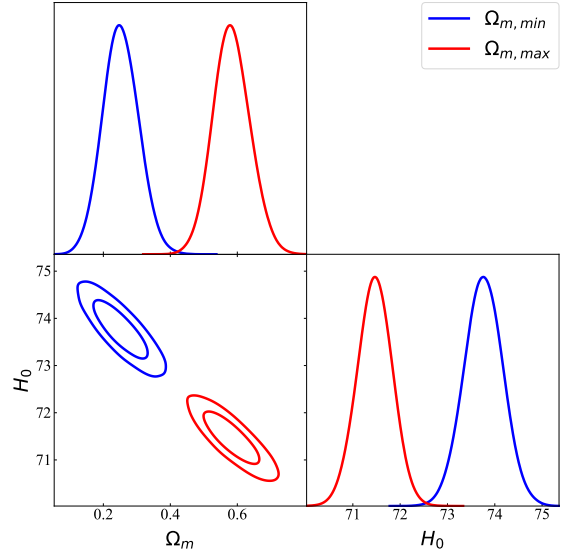


**Fig. 8.** Confidence contours ( $1\sigma$  and  $2\sigma$ ) and marginalized likelihood distributions for the parameters space ( $\Omega_m$  and  $H_0$ ) in the spatially flat  $\Lambda$ CDM model from the SNe Ia subsamples which corresponds to  $\Omega_{m,\min}$  (blue line) and  $\Omega_{m,\max}$  (red line). The best fitting results of preferred direction are  $\Omega_{m,\min} = 0.25^{+0.05}_{-0.05}$  and  $H_0 = 73.76^{+0.41}_{-0.41} \text{ km s}^{-1} \text{ Mpc}^{-1}$  (blue line). The best fitting results of opposite direction are  $\Omega_{m,\max} = 0.58^{+0.06}_{-0.05}$  and  $H_0 = 71.46^{+0.37}_{-0.37} \text{ km s}^{-1} \text{ Mpc}^{-1}$  (red line).

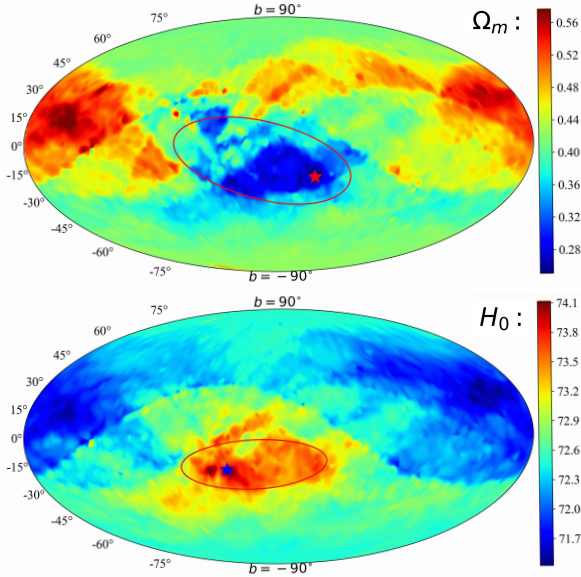


**Fig. 7.** All-sky distribution of the cosmological parameters utilizing the  $z < 0.30$  part of Pantheon+ sample (lp+ sample) combined with the  $90^\circ$  RF method. The left and the right panel show the results of  $\Omega_m$  and  $H_0$ , respectively. The corresponding values of  $D_{\max}(\sigma)$  are  $4.17\sigma$  and  $4.49\sigma$ , respectively. The star marks the directions of the lowest  $\Omega_m$  (left panel) and the largest  $H_0$  (right panel), and the red circle outlines the corresponding  $1\sigma$  areas. The directions and  $1\sigma$  areas are parameterized as  $\Omega_m (26.4^{+26.3}_{-100.9}, -19.3^{+35.4}_{-17.0})$ ,  $H_0 (321.9^{+72.5}_{-33.5}, -18.9^{+16.6}_{-11.5})$ .

the local matter underdensity and cosmic anisotropy given by the reanalyses using the lp+ sample are

$$(l, b) = (26.4^{+26.3}_{-100.9}, -19.3^{+35.4}_{-17.0}), \quad (10)$$

and

$$(l, b) = (321.9^{+72.5}_{-33.5}, -18.9^{+16.6}_{-11.5}). \quad (11)$$

The constraints corresponding to preferred directions of the local matter underdensity and cosmic anisotropy are ( $\Omega_{m,\min} = 0.25 \pm 0.05$  and  $H_0 = 73.76 \pm 0.41 \text{ km s}^{-1} \text{ Mpc}^{-1}$ ) and ( $H_{0,\max} = 74.11^{+0.47}_{-0.48} \text{ km s}^{-1} \text{ Mpc}^{-1}$  and  $\Omega_m = 0.27 \pm 0.06$ ). In Fig. 8, we show the confidence contours in the preferred and opposite directions of the local matter underdensity. The isotropic statistical results from the lp+ sample are shown in Fig. 9. For the Isotropy analysis, the statistical significance of the real data are  $3.68\sigma$  for  $\Omega_m$  anisotropy (upper, purple panel) and  $3.01\sigma$  for  $H_0$  anisotropy (upper, blue panel). The Isotropy (RP) analysis gives the statistical significance of the real data which are  $2.09\sigma$  for  $\Omega_m$  anisotropy (lower, purple panel) and  $1.35\sigma$  for  $H_0$  anisotropy (lower, blue panel).

#### 4.2. Different screening angles $\theta_{\max}$

Theoretically, if there are enough SNe data distributed at different redshift in a certain direction, the constraints of the cosmological parameters in this direction can be obtained (Lin et al. 2016a; Deng & Wei 2018b; Kumar Aluri et al. 2023). Due to the limitation of the number of observational data, it is currently impossible to directly give the result of the limitation of cosmological parameters in a certain direction. Therefore, the  $90^\circ$  RF method is usually used to derive the cosmological constraint of the single direction, i.e., hemisphere comparison (HC) method (Schwarz & Weinhorst 2007). In this subsection, we try to find out the limit value of  $\theta_{\max}$  which is suitable for the Pantheon+ sample by mapping the all-sky distributions of the cosmological parameters  $\Omega_m$  and  $H_0$  with different  $\theta_{\max}$ . Considering the limitations of computing time, only three angles ( $30^\circ$ ,  $45^\circ$  and  $60^\circ$ ) are chosen. Take  $\hat{D} (60^\circ, 0^\circ)$  as an example, Figure 10 shows the schematic diagram of the RF method with different  $\theta_{\max}$ . Smaller  $\theta_{\max}$  will reduce the overlapping data between sub-samples generated by adjacent random directions. The corresponding all-sky distributions will present more details on the current state of the

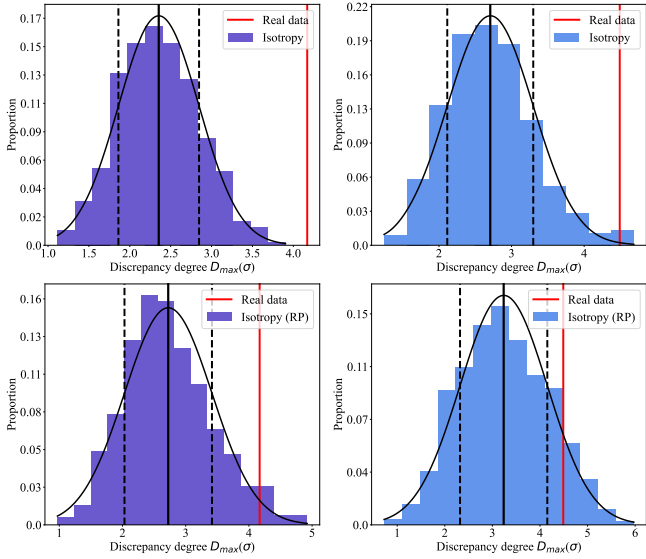


**Fig. 9.** Distribution of the discrepancy degree  $D_{\max}$  in 500 simulated isotropic datasets. The upper two panels show the results of statistical isotropic analyses (Isotropy). The lower two panels show the results of statistical isotropic analyses that preserve the spatial inhomogeneity of real data (Isotropy (RP)). The purple and blue represent the statistical results of  $\Omega_m$  and  $H_0$ . The black curve is the best fitting to the Gaussian function. The solid black and vertical dashed lines are commensurate with the mean and the standard deviation, respectively. The red lines represent the discrepancy degree from the real data. For the Isotropy analyses, the statistical significance of the real data are  $3.68\sigma$  for  $\Omega_m$  anisotropy;  $3.01\sigma$  for  $H_0$  anisotropy. For the Isotropy (RP) analyses, the statistical significance of the real data are  $2.09\sigma$  and  $1.35\sigma$  for  $\Omega_m$  and  $H_0$  anisotropy, respectively.

Universe. For the Pantheon+ sample, lowering  $\theta_{\max}$  can be expected to produce some poorly fitting results. Therefore we give a constrained culling of possibly poorly constraints. Here we set a loose condition  $0 < \Omega_m < 1.00$ . The final results are shown in Fig. A.1. For the screening angles  $30^\circ$ ,  $45^\circ$  and  $60^\circ$ , the proportions of the wrong fitting results are 30.34%, 6.47% and 0.70%, respectively. From Fig. A.1, we find that  $\theta_{\max} = 60^\circ$  seems to be the limit that the Pantheon+ sample can bear. At this time, nearly 100% (99.30%) of the random directions ( $\hat{D}$ ) can be reliably constrained.

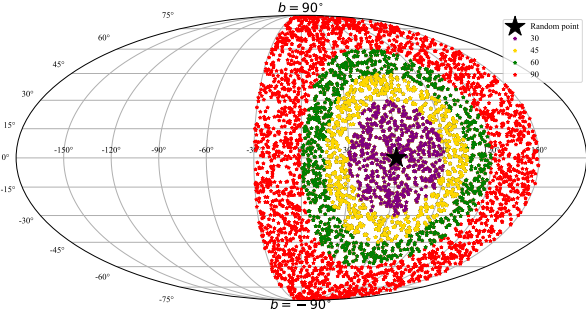


**Fig. 10.** The schematic diagram of the hemisphere method with different screening angles including  $30^\circ$ ,  $45^\circ$ ,  $60^\circ$  and  $90^\circ$ . Black star represent the random direction  $\hat{D}$  ( $60^\circ$ ,  $0^\circ$ ).

In Fig. A.2, we give the best fits for the hemispheres where  $\Omega_{m,\min}$  and  $\Omega_{m,\max}$  are located. We can find that taking into account narrowing the screening angle  $\theta_{\max}$  significantly increases the  $1\sigma$  error of  $\Omega_m$  constraints. The reduced chi-square ( $\chi_r^2$ ) cor-

responding to  $\Omega_{m,\min}$  is 0.69, which is much smaller than 1.00. Therefore we only show the analysis results of  $H_0$ . The all-sky distribution, cosmological constraints and isotropic statistical results are displayed in Figs. 11, 12 and 13, respectively. As shown in Fig. 11, the preferred direction of cosmic anisotropy given by the  $H_0$  distribution is  $(351.4^{+28.0}_{-64.2}, -8.8^{+40.3}_{-27.8})$ , and  $D_{\max}$  is  $4.39\sigma$ . The corresponding constraints of preferred direction are  $H_{0,\max} = 74.81^{+0.71}_{-0.71} \text{ km s}^{-1} \text{ Mpc}^{-1}$  and  $\Omega_m = 0.28^{+0.05}_{-0.04}$ . The statistical isotropy results show that the statistical confidence of the real data are  $1.70\sigma$  for the Isotropy analysis, and  $2.38\sigma$  for the Isotropy (RP) analysis.

All results in this section are summarized in Tab. 1. Additionally we provide the reduced chi-square  $\chi_r^2$  for the anisotropic direction.

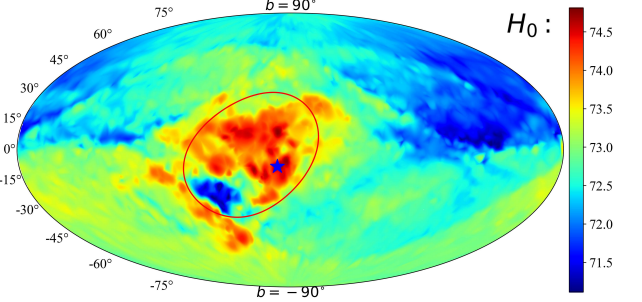


**Fig. 11.** All-sky distribution of  $H_0$  utilizing the Pantheon+ sample combined with the  $60^\circ$  RF method. The direction and  $1\sigma$  area are parameterized as  $(351.4^{+28.0}_{-64.2}, -8.8^{+40.3}_{-27.8})$ . The statistical discrepancy  $D_{\max}$  is  $4.39\sigma$ .

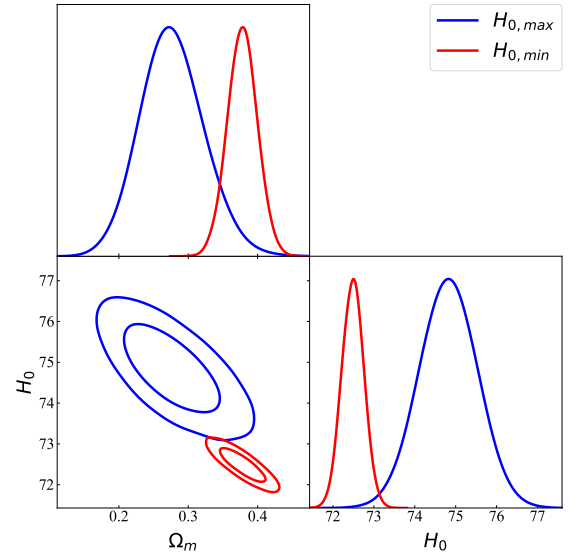


**Fig. 12.** Confidence contours ( $1\sigma$  and  $2\sigma$ ) and marginalized likelihood distributions for the parameters space ( $\Omega_m$  and  $H_0$ ) in the spatially flat  $\Lambda$ CDM model from the SNe Ia subsamples which corresponds to  $H_{0,\min}$  (red line) and  $H_{0,\max}$  (blue line). The best fitting results of preferred direction are  $H_{0,\max} = 74.81^{+0.71}_{-0.71} \text{ km s}^{-1} \text{ Mpc}^{-1}$  and  $\Omega_m = 0.28^{+0.05}_{-0.04}$  (blue line). The best fitting results of opposite direction are  $H_{0,\min} = 72.49^{+0.27}_{-0.27} \text{ km s}^{-1} \text{ Mpc}^{-1}$  and  $\Omega_m = 0.38^{+0.02}_{-0.02}$  (red line).

## 5. Discussion

All-sky distributions of cosmological parameters ( $\Omega_m$  and  $H_0$ ) from the total sample show that there is an obvious local under-



**Table 1.** Detailed information of analysis results from the all-sky distribution of cosmological parameters.

Sample	$\theta_{\max}^a$	$\Omega_{m,min}$	$H_0$ (km s <sup>-1</sup> Mpc <sup>-1</sup> )	$D_{\max}^b$ ( $\sigma$ )	$\alpha^c$ ( $\sigma$ )	$\beta^d$ ( $\sigma$ )	Direction (l, b)	$\chi_r^2$
Pantheon+	90°	$0.29^{+0.03}_{-0.02}$	$74.11^{+0.40}_{-0.40}$	3.29	2.78	2.34	$(308.4^{+47.6}_{-48.7}, -18.2^{+21.1}_{-28.8})$	0.94
Pantheon+	60°	$0.23^{+0.20}_{-0.17}$	$74.05^{+1.00}_{-1.00}$	-	-	-	-	0.69*
lp+	90°	$0.25^{+0.05}_{-0.05}$	$73.76^{+0.41}_{-0.41}$	4.17	3.68	2.09	$(26.4^{+26.3}_{-100.9}, -19.3^{+35.4}_{-17.0})$	0.94
Sample	$\theta_{\max}^a$	$H_{0,max}$ (km s <sup>-1</sup> Mpc <sup>-1</sup> )	$\Omega_m$	$D_{\max}^b$ ( $\sigma$ )	$\alpha^c$ ( $\sigma$ )	$\beta^d$ ( $\sigma$ )	Direction (l, b)	$\chi_r^2$
Pantheon+	90°	$74.26^{+0.40}_{-0.39}$	$0.30^{+0.03}_{-0.03}$	4.48	3.96	3.15	$(313.4^{+19.6}_{-18.2}, -16.8^{+11.1}_{-10.7})$	0.98
Pantheon+	60°	$74.81^{+0.71}_{-0.71}$	$0.28^{+0.05}_{-0.04}$	4.39	1.70	2.38	$(351.4^{+28.0}_{-64.2}, -8.8^{+40.3}_{-27.8})$	0.99
lp+	90°	$74.11^{+0.47}_{-0.48}$	$0.27^{+0.06}_{-0.06}$	4.49	3.01	1.35	$(321.9^{+72.5}_{-33.5}, -18.9^{+16.6}_{-11.5})$	1.14

<sup>a</sup>  $\theta_{\max}$  is the screening angle.

<sup>b</sup>  $D_{\max}$  represents the degree of deviation from the cosmological principle, and the larger the value, the higher the degree of deviation.

<sup>c</sup>  $\alpha$  indicates the statistical significance of real data from the Isotropy analysis.

<sup>d</sup>  $\beta$  indicates the statistical significance of real data from the Isotropy (RP) analysis.

\* For the RF (60°) results of the Pantheon+ sample, the reduced chi-square ( $\chi_r^2$ ) corresponding to  $\Omega_{m,min}$  is 0.69, which is much smaller than 1.00. Therefore, the RF (60°) results are not given.

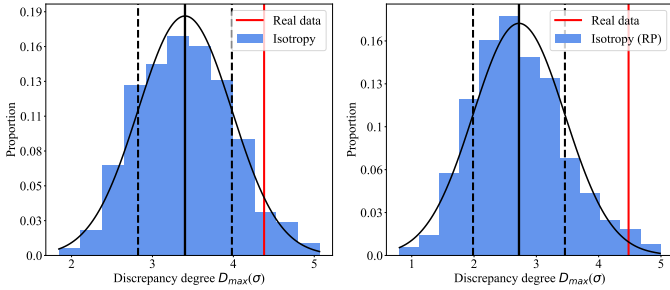


**Fig. 13.** Distribution of the discrepancy degree  $D_{\max}$  obtained from the  $H_0$  distribution in 500 simulated isotropic datasets. The left panel and right panel show the results of Isotropy and Isotropy (RP) analyses, respectively. The black curve is the best fitting to the Gaussian function. The solid black and vertical dashed lines are commensurate with the mean and the standard deviation, respectively. The red lines represent the discrepancy degree from the real data. The statistical significance of the real data are  $1.70\sigma$  for the Isotropy analysis and  $2.38\sigma$  for the Isotropy (RP) analysis.

density area and a preferred direction of cosmic expansion. From Fig. 3, we can find that there are some weird features which may result from fluctuations in the matter density, or fluctuations in the Hubble expansion (Gurzadyan, V. G. et al. 2023). In the upper panel, the red and blue areas represent areas of higher and lower material density, respectively. In the lower panel, the red areas represent regions of higher Hubble expansion. The continuity of these structures suggests that the results may not be sensitive to individual SNe Ia. Combining these two panels of Fig. 3, we find that the local underdensity in the upper panel overlaps with the higher Hubble expansion (cosmic anisotropy) in the lower panel. This may imply that local matter density might be responsible for the anisotropy of the accelerated expansion of the universe. The corresponding  $1\sigma$  regions are quite obvious, i.e. the  $1\sigma$  range of  $\Omega_m$  is significantly larger than that of  $H_0$ . The main reason for this phenomenon might be that these two parameters have different sensitivities on the redshift. The inhomogeneous matter-density distribution could also affect the deceleration parameter  $q_0$ , causing a larger  $q_0$  in the local underdensity. Theoretically, the maximum  $q_0$  direction should be consistent with the local underdensity direction. For the determination of

$H_0$  value with local distance indicators, the observed  $H_0$  values depend on the average matter density within the distance range covered (Böhringer et al. 2020). Combining the  $\Omega_m$  distribution, we can find that there might be a region of low matter density, which leads to a smaller average matter density which makes the  $H_0$  measurements higher. Therefore, the local underdensity can exacerbate the magnitude of the Hubble Tension (Böhringer et al. 2020; Hu & Wang 2022b; Jia et al. 2023; Hu & Wang 2023). In other words, accounting for the local underdensity or cosmic anisotropy could alleviate the current Hubble Tension.

From Fig. 5, we can find that the Isotropy analysis shows an obvious statistical significance, especially the study of  $H_0$ , which is nearly  $4\sigma$ . Afterwards, considering the spatial inhomogeneity of the real sample, we perform the Isotropy (RP) analysis and find a slight decrease in statistical significance. This suggests that inhomogeneous spatial distribution of real sample can increase the deviation from isotropy. In addition, combining all the statistical results, we find the statistical significations of  $H_0$  anisotropy are more obvious than that of  $\Omega_m$  anisotropy. From the distributions of a single parameter, we find an obvious anisotropy. But the effect of each other might be cancel out, making the all-sky distribution of luminosity distances isotropic. Therefore, in order to clear up this doubt, we plot the all-sky distribution of luminosity distances when  $z$  is set to 2.26, and give the relationships between  $d_L$  and  $z$  of two anisotropic hemispheres, as shown in Figs. 14 and 15 respectively. The results of these two figures show that the all-sky distribution of luminosity distances is also anisotropic and the  $d_L - z$  relationships obtained from two anisotropic hemispheres have obvious difference. And the direction of larger luminosity distance is consistent with the anisotropy direction from the Pantheon+ sample. All in all, our investigations from the Pantheon+ sample display a inhomogeneous and anisotropic universe, and the statistical results show not low confidence level.

Motivated by the recently researches (Krishnan et al. 2020, 2021b; Dainotti et al. 2021, 2022a; Colgáin et al. 2022; Hu & Wang 2022b; Ó Colgáin et al. 2022; Jia et al. 2023; Malekjani et al. 2023) which hints that  $H_{0,z}$  might evolve with redshift, we make reanalyses using the low-redshift (lp+) sample. If the evolution of  $H_{0,z}$  with redshift, which may be caused by the local void, etc., really exists, i.e. the measured  $H_0$  of low-redshift and



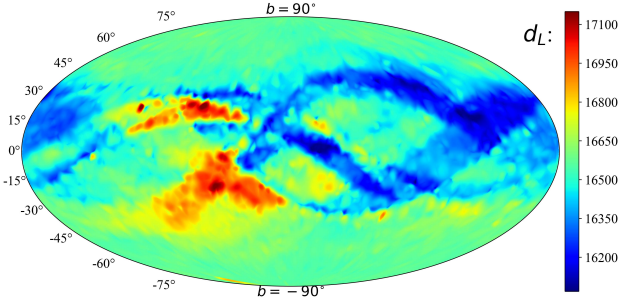


**Fig. 14.** All-sky distribution of luminosity distance  $d_L$  utilizing the Pantheon+ sample combined with the  $90^\circ$  RF method. Here, we fix  $z = 2.26$ .

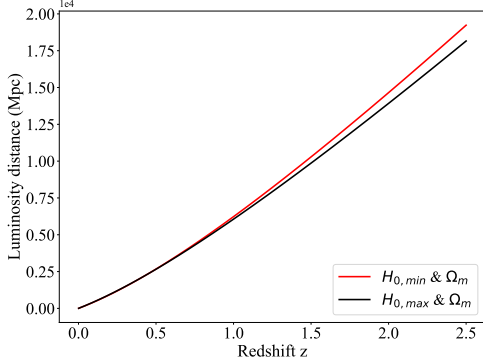


**Fig. 15.** Relationships between  $d_L$  and  $z$  of two anisotropic hemispheres using the two sets of best fits ( $H_{0,min}, \Omega_m$ ) and ( $H_{0,max}, \Omega_m$ ) in the  $H_0$  distribution.

high-redshift SNe samples are different. In that case, if the redshift distribution is not uniform across the sky, this could create biases in the anisotropy detection, especially when the full sample is used, and the redshift range is wider. The value of  $H_0$  obtained from the higher redshift hemisphere is smaller than that obtained from the lower redshift hemisphere. Severe redshift uneven distribution might lead to an increase in the degree of anisotropy or a biases in the anisotropy detection. The reanalysis results are similar to that of the Pantheon+ sample, and verify our previous findings. From the results of lp+ sample (Fig. 7), we find that directions of the local matter underdensity and cosmic anisotropy given by the lp+ sample are inconsistent. Comparing the results in Figs. 4 and 8, we can find that the best fits of the two anisotropic hemispheres obtained from the lp+ sample are significantly worse than the results of the total sample. In Fig. 16, we also show the relationship between  $D_{max}$  and  $z_{max}$ , the detailed information are display in Tab. 2. From Fig. 16, we can find that  $D_{max}$  changes with  $z_{max}$ , and has a maximum value near  $z_{max} = 0.30$ . This might imply that the structure of the universe changes with redshift. In addition, we also find that the influence of redshift on the all-sky distribution of  $\Omega_m$  is larger than that of  $H_0$ . Finally, from the statistical results of lp+ sample, we also find that the statistical significance obtained from Isotropy (RP) analysis are lower than that from the Isotropy analysis. This finding confirm that inhomogeneous spatial distribution of real sample can increase the deviation from isotropy.

Theoretically, the screening angle  $\theta_{max}$  in the RF method can be any value between  $(0^\circ, 180^\circ)$ . However, due to the limitations of real data in quantity, spatial part and redshift distribution,  $\theta_{max}$  cannot be selected arbitrarily. In Sec. 4.2, we combine the RF method with the latest Pantheon+ sample, hoping to find

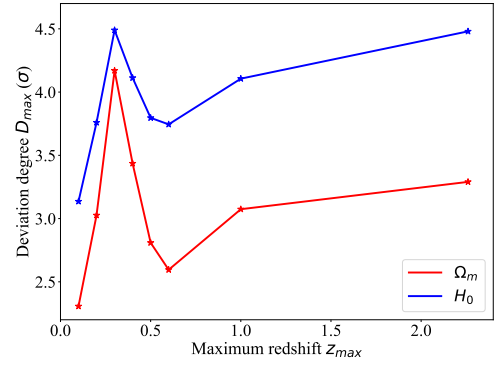


**Fig. 16.** Relationship between the discrepancy degree  $D_{max}$  and  $z_{max}$ .

**Table 2.** Detail information on the investigation of relationship between the discrepancy degree  $D_{max}$  and  $z_{max}$ .

$z_{max}$	Number	$D_{max}(\Omega_m)$ ( $\sigma$ )	$D_{max}(H_0)$ ( $\sigma$ )
0.10	747	2.31	3.14
0.20	962	3.03	3.76
0.30	1218	4.17	4.49
0.40	1399	3.43	4.11
0.50	1497	2.81	3.80
0.60	1575	2.60	3.74
1.00	1677	3.07	4.11
2.26	1701	3.29	4.48

\*  $D_{max}$  represents the degree of deviation from the cosmological principle, and the larger the value, the higher the degree of deviation.

a suitable screening angle  $\theta_{max}$ . The analysis results are shown in Fig. A.1. Finally, we find that the screening angle  $\theta_{max}$  of the Pantheon+ sample is  $60^\circ$ . Then based on the  $60^\circ$  RF method, we restudy the Pantheon+ sample. The corresponding results are shown in Figs. 11, 12 and 13. From Fig. 11, we can find that there is a small area ( $314.16^\circ, -22.92^\circ$ ) with lower  $H_0$  value in the higher  $H_0$  area, but this structure does not appear in the RF ( $90^\circ$ ) results. The lower  $H_0$  area may be caused by high material density structures (for example dark matter halo) or statistical uncertainty. Narrowing the screening angle reduces the number of SNe constraining cosmological parameters, which may increase the uncertainty of the constraint. We perform a bootstrap resampling of the sample (ignoring the direction, repeated 2000 times) to study the dependence of best-fit result error and  $D_{max}$  on the number of SNe Ia used. Here, the number of SNe ranges from 100 to 700, with a total of seven groups. From the results of Fig. 17, we can find that the average error and  $D_{max}$  increases as the used number of SNe decreases. The number of used SNe significantly affects the average error but does not significantly affect the  $D_{max}$  value. The  $D_{max}$  difference caused by the reduction in number is much smaller than the total  $D_{max}$ . The preferred direction of cosmic anisotropy using the RF method with  $\theta_{max} = 60^\circ$  is in line with that using  $\theta_{max} = 90^\circ$  within  $1\sigma$  error. But narrowing the screening angle, the statistical significance of isotropy analyses are significantly reduced. Interestingly, unlike previous findings, the statistical significance of the isotropy (RP) analysis is actually higher than that of Isotropy.

Overall, we find that the all-sky distributions of cosmological parameters deviate significantly from isotropy, as shown in Figs. 3, 7 and 11. All preferred directions we obtained are con-

sistent with each other within  $1\sigma$  range, and they are in line with previous researches that traced the anisotropy of  $\Omega_m$  and  $H_0$  (Antoniou & Perivolaropoulos 2010; Cai & Tuo 2012; Kalus et al. 2013; Chang & Lin 2015; Hu et al. 2020) and other dipole researches Wang & Wang (2014); Yang et al. (2014); Lin et al. (2016b); Chang & Zhou (2019). But they are different from Luongo et al. (2022) and McConville & Colgáin (2023) which are consistent with the results of CMB dipole (Planck Collaboration et al. 2016, 2020a). In addition, comparing with other independent observations (as shown in Table 3) including the CMB dipole (Planck Collaboration et al. 2016, 2020a), dark flow (Abdalla et al. 2022), bulk flow (Turnbull et al. 2012; Feix et al. 2017; Watkins et al. 2023) and galaxy cluster (Migkas et al. 2021), it is easy to find that the directions of the larger  $H_0$  and the smaller  $\Omega_m$  are not consistent with the CMB dipole (Planck Collaboration et al. 2016, 2020a), but coincides with the bulk flow (Turnbull et al. 2012; Feix et al. 2017; Watkins et al. 2023) and the galaxy cluster (Migkas et al. 2021). To make it easier to understand, we aggregated these results with the ones we got, marking them on the galactic coordinate system, as shown in Fig. 18. The effect of peculiar velocities and the bulk flow on SNe Ia cosmology has been discussed earlier (Hui & Greene 2006; Davis et al. 2011; Betoule et al. 2014; Rameez et al. 2018). They can make a tiny shift in the best-fit cosmological parameters and the preferred direction locally (Colin et al. 2019).

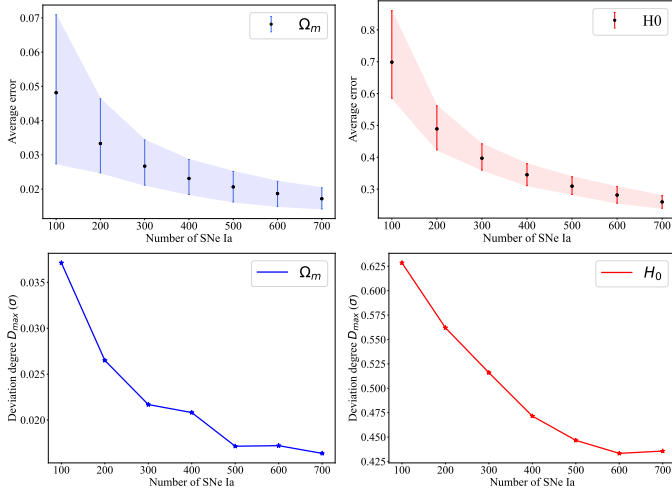


**Fig. 17.** Relationship between the average error and the discrepancy degree  $D_{\max}$  and the used SNe number. The upper panels show the relationship between the average error and the used SNe number. The lower panels show the relationship between the discrepancy degree  $D_{\max}$  and the used SNe number. Blue and red correspond to parameters  $\Omega_m$  and  $H_0$  respectively.

## 6. Conclusions and perspectives

In this paper, we propose the region fitting (RF) method for the first time, and combine this method with the Pantheon+ sample to test the cosmological principle. From the matter density and the Hubble expansion distributions which mapped by employing the RF method, we find that the all-sky distributions of cosmological parameters deviate significantly from isotropy. The corresponding distribution of luminosity distance also deviates from isotropy, i.e. the  $d_L$ - $z$  relation actually diverges from region to region. Results of statistical isotropy analyses (Isotropy and Isotropy (RP)) show relatively high confidence,  $2.78\sigma$  (Isotropy) and  $2.34\sigma$  (Isotropy (RP)) for the local matter

underdensity,  $3.96\sigma$  (Isotropy) and  $3.15\sigma$  (Isotropy (RP)) for the cosmic anisotropy. Comparing the results of statistical isotropy analyses, we find that inhomogeneous spatial distribution of real sample can increase the deviation from isotropy. The statistical significations of  $H_0$  anisotropy are more obvious than that of  $\Omega_m$  anisotropy. This might hint that parameter  $H_0$  is more sensitive to cosmic anisotropy. The similar results and findings are found from reanalyses of the low-redshift sample (lp+) and the lower screening angle ( $\theta_{\max} = 60^\circ$ ), but with a slight decrease in statistical significance. In addition, we also find that  $D_{\max}$  changes with  $z_{\max}$ , and has a maximum value near  $z_{\max} = 0.30$ . The average error and  $D_{\max}$  increases as the used number of SNe decreases. Comparing with the previous researches, we find all preferred directions we obtained are in line with that provided by Antoniou & Perivolaropoulos (2010); Cai & Tuo (2012); Wang & Wang (2014); Yang et al. (2014); Kalus et al. (2013); Chang & Lin (2015); Lin et al. (2016b); Chang & Zhou (2019); Hu et al. (2020), but not consistent with that given by Luongo et al. (2022); McConville & Colgáin (2023).

Until now, many SNe Ia have been observed and have been widely used for cosmological applications (Hoscheit & Barger 2018; Perivolaropoulos & Skara 2021; Cowell et al. 2022; Hu & Wang 2022a; Wang 2022; Briffa et al. 2023).<sup>4</sup> However, there is still an inhomogeneous distribution in data, which significantly affects the testing of cosmological principle. In order to solve this problem, one way is to add some new SNe Ia measurements, another way is to consider other independent observations, for example quasar (Lusso & Risaliti 2016; Bisogni et al. 2017; Lusso & Risaliti 2017; Risaliti & Lusso 2019; Cao et al. 2022b; Khadka et al. 2022; Liu et al. 2023a; Zajaček et al. 2023), gamma-ray burst (GRB; Wang et al. 2015; Hu et al. 2021; Cao et al. 2022a; Liu et al. 2022b; Liang et al. 2022; Wang et al. 2022), fast radio burst (FRB; Hagstotz et al. 2022; Wu et al. 2022; James et al. 2022; Zhao et al. 2022; Gao et al. 2023; Liu et al. 2023b), Tip of the Red Giant Branch (TRGB; Freedman et al. 2019, 2020; Freedman 2021), galaxy cluster (Javanmardi & Kroupa 2017; Migkas et al. 2020, 2021), gravitational wave (GW; Abbott et al. 2017; Chen et al. 2018; Jin et al. 2023; Wang et al. 2023), etc. At present, these observations may still have some deficiencies in quantity or quality, but this situation is expected to improve in the future. The e-ROSITA all-sky survey (Merloni et al. 2012; Predehl 2012; Kolodzig et al. 2013; Lusso 2020), Einstein Probe (EP) (Yuan et al. 2015), French–Chinese satellite space-based multi-band astronomical variable objects monitor (SVOM) (Wei et al. 2016), China Space Station Telescope (CSST) photometric survey (Xu et al. 2022; Miao et al. 2023; Li et al. 2023a), Transient High-Energy Sky and Early Universe Surveyor (THESEUS) (Amati et al. 2018) space missions together with ground- and space-based multi-messenger facilities will provide a lot of observations/measurements, improve the observational quality, probe the poorly explored high-redshift universe. The Australian Square Kilometer Array Pathfinder (ASKAP; Chapman et al. 2017), MeerKAT (Sanidas et al. 2018), Very Large Array (VLA; Law et al. 2018) and Canadian Hydrogen Intensity Mapping Experiment (CHIME)/FRB Outriggers (Leung et al. 2021) will provide a large number of positioned FRBs in the future,

<sup>4</sup> More recent studies on the Cosmological applications employing the SNe Ia sample see Bargiacchi et al. (2023); Cao & Ratra (2023); de Jaeger & Galbany (2023); Jin et al. (2023); Mandal et al. (2023); Ó Colgáin et al. (2023); Pastén & Cárdenas (2023); Perivolaropoulos & Skara (2023); Sakr (2023); Van Raamsdonk & Waddell (2023); Wang & Chen (2023) and references therein.

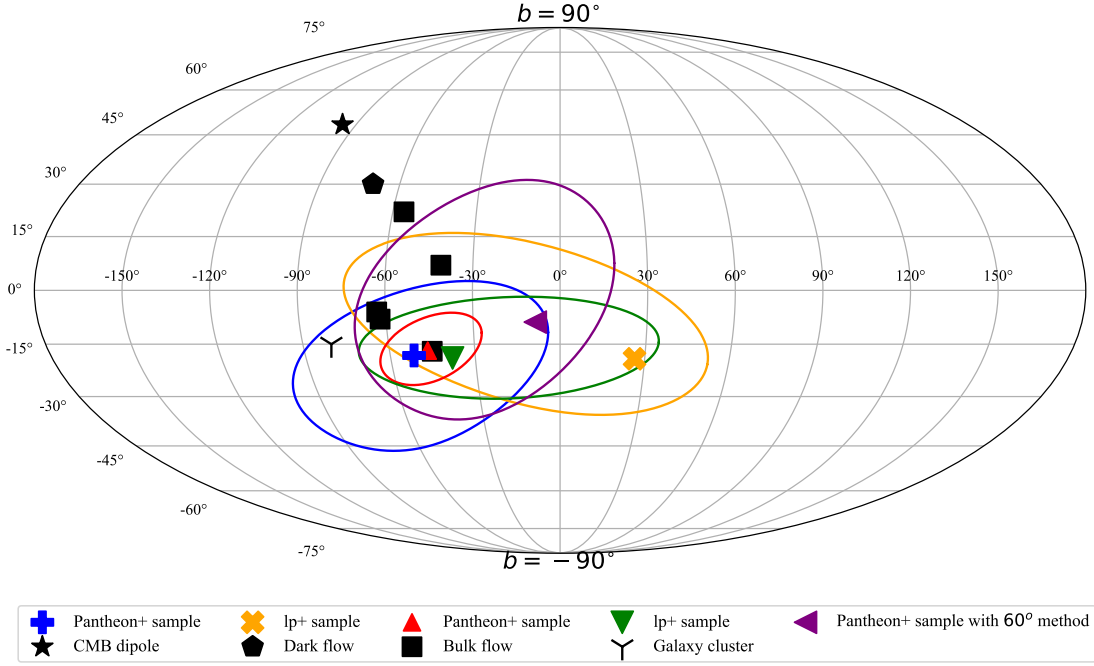


**Fig. 18.** Distribution of the preferred directions ( $l, b$ ) with  $1\sigma$  range in other independent observations. We mark the directions given by  $\Omega_m$  with plus signs at different screening angles, and the directions given by  $H_0$  with triangles at different screening angles. The color is the important result obtained in this paper, and the black color is the result given by other independent observations including the CMB dipole (Planck Collaboration et al. 2016, 2020a), dark flow (Abdalla et al. 2022), bulk flow (Turnbull et al. 2012; Feix et al. 2017; Watkins et al. 2023) and galaxy cluster (Migkas et al. 2021).

**Table 3.** Preferred directions given by other independent observations.

Cosmological obs.	Direction ( $l, b$ )	Ref.
CMB dipole	$(264.00^\circ \pm 0.03, 48.24^\circ \pm 0.02)$	(Planck Collaboration et al. 2016)
	$(264.02^\circ \pm 0.01, 48.25^\circ \pm 0.01)$	(Planck Collaboration et al. 2020a)
Dark flow	$(290^\circ \pm 20, 30^\circ \pm 15)$	(Abdalla et al. 2022)
Bulk flow	$(319^\circ \pm 18, 7^\circ \pm 14)$	(Turnbull et al. 2012)
	$(315^\circ \pm 52, -17^\circ \pm 15)$	(Feix et al. 2017)
	$(304^\circ \pm 14, 22^\circ \pm 11)$	(Feix et al. 2017)
	$(297^\circ \pm 4, -6^\circ \pm 3)$	(Watkins et al. 2023)
Galaxy cluster	$(298^\circ \pm 5, -8^\circ \pm 4)$	(Watkins et al. 2023)
	$(280^\circ \pm 35, -15^\circ \pm 20)$	(Migkas et al. 2021)
Pantheon+ ( $90^\circ$ )	$(313.4^{+19.6}_{-18.2}, -16.8^{+11.1}_{-10.7})$	this paper
Pantheon+ ( $60^\circ$ )	$(351.4^{+28.0}_{-64.2}, -8.8^{+40.3}_{-27.8})$	this paper
lp+ ( $90^\circ$ )	$(321.9^{+72.5}_{-33.5}, -18.9^{+16.6}_{-11.5})$	this paper

which will provide higher-precision cosmological constraints. In addition, the Advanced Laser Interferometer Gravitational-wave Observatory (aLIGO; LIGO Scientific Collaboration et al. 2015) and Virgo (Acernese et al. 2015) detectors will provide more GW events. In combination with the electromagnetic counterparts, model-independent constraints will be given on the cosmological parameters. The high-quality observations enable us to examine cosmological principle at higher redshifts and investigate whether the Hubble tension is related to the failure of the cosmological principle.

*Notes:* When this work is about to be completed, Perivolaropoulos (2023) used the HC method to test the cosmic isotropy of the SNe Ia absolute magnitudes from the Pantheon+ and SH0ES samples in various redshift/distance bins. They found that sharp changes of the level of anisotropy occurring at distances less than 40 Mpc in the real samples. If there exists enough local ob-

servations in the future, more local information about our Universe could be obtained combining our method with the idea of Perivolaropoulos (2023). This will be pursued in future work.

## Acknowledgements

We thank the anonymous referee for constructive comments. This work was supported by the National Natural Science Foundation of China (grant No. 12273009), the China Manned Space Project (CMS-CSST-2021-A12), Jiangsu Funding Program for Excellent Postdoctoral Talent (20220ZB59), Project funded by China Postdoctoral Science Foundation (2022M721561), NWO, the Dutch Research Council, under Vici research programme ‘ARGO’ with project number 639.043.815, Yunnan Youth Basic Research Projects 202001AU070013 and

National Natural Science Foundation of China (grant No. 12303050).

## References

- Abbott, B. P., Abbott, R., Abbott, T. D., et al. 2017, *Nature*, 551, 85
- Abbott, T. M. C., Alarcon, A., Allam, S., et al. 2019, *Phys. Rev. Lett.*, 122, 171301
- Abdalla, E., Abellán, G. F., Aboubrahim, A., et al. 2022, *Journal of High Energy Astrophysics*, 34, 49
- Acernese, F., Agathos, M., Agatsuma, K., et al. 2015, *Classical and Quantum Gravity*, 32, 024001
- Akarsu, Ö., Barrow, J. D., & Uzun, N. M. 2020, *Phys. Rev. D*, 102, 124059
- Akarsu, Ö., Dereli, T., & Katirci, N. 2022, in *Journal of Physics Conference Series*, Vol. 2191, *Journal of Physics Conference Series*, 012001
- Akarsu, Ö., Di Valentino, E., Kumar, S., Özyigit, M., & Sharma, S. 2023, *Physics of the Dark Universe*, 39, 101162
- Amati, L., O'Brien, P., Götz, D., et al. 2018, *Advances in Space Research*, 62, 191
- Andrade, U., Bengaly, C. A. P., Santos, B., & Alcaniz, J. S. 2018, *ApJ*, 865, 119
- Antoniou, I. & Perivolaropoulos, L. 2010, *J. Cosmology Astropart. Phys.*, 2010, 012
- Bargiacchi, G., Dainotti, M. G., Nagataki, S., & Capozziello, S. 2023, *MNRAS*, 521, 3909
- Bayron Orjuela-Quintana, J., Álvarez, M., Valenzuela-Toledo, C. A., & Rodríguez, Y. 2020, *J. Cosmology Astropart. Phys.*, 2020, 019
- Bennett, C. L., Halpern, M., Hinshaw, G., et al. 2003, *ApJS*, 148, 1
- Bennett, C. L., Hill, R. S., Hinshaw, G., et al. 2011, *ApJS*, 192, 17
- Bennett, C. L., Larson, D., Weiland, J. L., et al. 2013, *ApJS*, 208, 20
- Betoule, M., Kessler, R., Guy, J., et al. 2014, *A&A*, 568, A22
- Bielewicz, P., Górski, K. M., & Banday, A. J. 2004, *MNRAS*, 355, 1283
- Bisogni, S., Risaliti, G., & Lusso, E. 2017, *Frontiers in Astronomy and Space Sciences*, 4, 68
- Böhringer, H., Chon, G., & Collins, C. A. 2020, *A&A*, 633, A19
- Bonvin, C., Durrer, R., & Kunz, M. 2006, *Phys. Rev. Lett.*, 96, 191302
- Briffa, R., Escamilla-Rivera, C., Said, J. L., & Mifsud, J. 2023, *MNRAS*, 522, 6024
- Brout, D., Sako, M., Scolnic, D., et al. 2019, *ApJ*, 874, 106
- Brout, D., Scolnic, D., Popovic, B., et al. 2022, *ApJ*, 938, 110
- Brown, P. J., Breeveld, A. A., Holland, S., Kuin, P., & Pritchard, T. 2014, *Ap&SS*, 354, 89
- Cai, R.-G., Ding, J.-F., Guo, Z.-K., Wang, S.-J., & Yu, W.-W. 2021, *Phys. Rev. D*, 103, 123539
- Cai, R.-G. & Tuo, Z.-L. 2012, *J. Cosmology Astropart. Phys.*, 2012, 004
- Cai, T., Ding, Q., & Wang, Y. 2022, *arXiv e-prints*, arXiv:2211.06857
- Camarena, D., Marra, V., Sakr, Z., & Clarkson, C. 2022, *Classical and Quantum Gravity*, 39, 184001
- Cao, S., Khadka, N., & Ratra, B. 2022a, *MNRAS*, 510, 2928
- Cao, S. & Ratra, B. 2022, *MNRAS*, 513, 5686
- Cao, S. & Ratra, B. 2023, *Phys. Rev. D*, 107, 103521
- Cao, S., Zajaček, M., Panda, S., et al. 2022b, *MNRAS*, 516, 1721
- Capozziello, S., Sarracino, G., & Spallicci, A. D. A. M. 2023, *Physics of the Dark Universe*, 40, 101201
- Carr, A., Davis, T. M., Scolnic, D., et al. 2022, *PASA*, 39, e046
- Castello, S., Högås, M., & Mörtzell, E. 2022, *J. Cosmology Astropart. Phys.*, 2022, 003
- Chang, Z. & Lin, H.-N. 2015, *MNRAS*, 446, 2952
- Chang, Z., Lin, H.-N., Zhao, Z.-C., & Zhou, Y. 2018, *Chinese Physics C*, 42, 115103
- Chang, Z. & Zhou, Y. 2019, *MNRAS*, 486, 1658
- Chapman, J. M., Dempsey, J., Miller, D., et al. 2017, in *Astronomical Society of the Pacific Conference Series*, Vol. 512, *Astronomical Data Analysis Software and Systems XXV*, ed. N. P. F. Lorente, K. Shortridge, & R. Wayth, 73
- Chen, H.-Y. 2019, *Nature Astronomy*, 3, 384
- Chen, H.-Y., Fishbach, M., & Holz, D. E. 2018, *Nature*, 562, 545
- Colgáin, E. Ó., Sheikh-Jabbari, M. M., Solomon, R., Dainotti, M. G., & Stojkovic, D. 2022, *arXiv e-prints*, arXiv:2206.11447
- Colin, J., Mohayaee, R., Rameez, M., & Sarkar, S. 2017, *MNRAS*, 471, 1045
- Colin, J., Mohayaee, R., Rameez, M., & Sarkar, S. 2019, *A&A*, 631, L13
- Colin, J., Mohayaee, R., Sarkar, S., & Shafieloo, A. 2011, *MNRAS*, 414, 264
- Cowell, J. A., Dhawan, S., & Macpherson, H. J. 2022, *arXiv e-prints*, arXiv:2212.13569
- Dainotti, M. G., De Simone, B., Schiavone, T., et al. 2021, *ApJ*, 912, 150
- Dainotti, M. G., De Simone, B. D., Schiavone, T., et al. 2022a, *Galaxies*, 10, 24
- Dainotti, M. G., Nielson, V., Sarracino, G., et al. 2022b, *MNRAS*, 514, 1828
- Davis, T. M., Hui, L., Frieman, J. A., et al. 2011, *ApJ*, 741, 67
- de Cruz Pérez, J., Park, C.-G., & Ratra, B. 2023, *Phys. Rev. D*, 107, 063522
- de Jaeger, T. & Galbany, L. 2023, *arXiv e-prints*, arXiv:2305.17243
- Deng, H.-K. & Wei, H. 2018a, *European Physical Journal C*, 78, 755
- Deng, H.-K. & Wei, H. 2018b, *Phys. Rev. D*, 97, 123515
- Dhawan, S., Borderies, A., Macpherson, H. J., & Heinesen, A. 2023, *MNRAS*, 519, 4841
- Di Valentino, E., Mena, O., Pan, S., et al. 2021, *Classical and Quantum Gravity*, 38, 153001
- Ebrahimian, E., Krishnan, C., Mondol, R., & Sheikh-Jabbari, M. M. 2023, *arXiv e-prints*, arXiv:2305.16177
- Enqvist, K. 2008, *General Relativity and Gravitation*, 40, 451
- Feix, M., Branchini, E., & Nusser, A. 2017, *MNRAS*, 468, 1420
- Ferreira, P. d. S. & Quartin, M. 2021, *Phys. Rev. D*, 104, 063503
- Foley, R. J., Scolnic, D., Rest, A., et al. 2018, *MNRAS*, 475, 193
- Foreman-Mackey, D., Hogg, D. W., Lang, D., & Goodman, J. 2013, *PASP*, 125, 306
- Freedman, W. L. 2021, *ApJ*, 919, 16
- Freedman, W. L., Madore, B. F., Hatt, D., et al. 2019, *ApJ*, 882, 34
- Freedman, W. L., Madore, B. F., Hoyt, T., et al. 2020, *ApJ*, 891, 57
- Ganeshalingam, M., Li, W., Filippenko, A. V., et al. 2010, *ApJS*, 190, 418
- Gao, J., Zhou, Z., Du, M., et al. 2023, *arXiv e-prints*, arXiv:2307.08285
- Garcia-Bellido, J. & Haugbølle, T. 2008, *J. Cosmology Astropart. Phys.*, 2008, 003
- Ghosh, S. & Jain, P. 2020, *MNRAS*, 492, 3994
- Ghosh, S., Kothari, R., Jain, P., & Rath, P. K. 2016, *J. Cosmology Astropart. Phys.*, 2016, 046
- Gruppuso, A., Finelli, F., Natoli, P., et al. 2011, *MNRAS*, 411, 1445
- Gurzadyan, V. G., Fimin, N. N., & Chechetkin, V. M. 2023, *A&A*, 677, A161
- Hagstotz, S., Reischke, R., & Lilow, R. 2022, *MNRAS*, 511, 662
- Hamaus, N., Aubert, M., Pisani, A., et al. 2022, *A&A*, 658, A20
- Hansen, F. K., Banday, A. J., & Górski, K. M. 2004, *MNRAS*, 354, 641
- Haslbauer, M., Banik, I., & Kroupa, P. 2020, *MNRAS*, 499, 2845
- Horstmann, N., Pietschke, Y., & Schwarz, D. J. 2022, *A&A*, 668, A34
- Hoscheit, B. L. & Barger, A. J. 2018, *ApJ*, 854, 46
- Hu, J. P. & Wang, F. Y. 2022a, *A&A*, 661, A71
- Hu, J. P. & Wang, F. Y. 2022b, *MNRAS*, 517, 576
- Hu, J.-P. & Wang, F.-Y. 2023, *Universe*, 9, 94
- Hu, J. P., Wang, F. Y., & Dai, Z. G. 2021, *MNRAS*, 507, 730
- Hu, J. P., Wang, Y. Y., & Wang, F. Y. 2020, *A&A*, 643, A93
- Hui, L. & Greene, P. B. 2006, *Phys. Rev. D*, 73, 123526
- Hutsemékers, D., Cabanac, R., Lamy, H., & Sluse, D. 2005, *A&A*, 441, 915
- Hwang, H. S., Geller, M. J., Park, C., et al. 2016, *ApJ*, 818, 173
- James, C. W., Ghosh, E. M., Prochaska, J. X., et al. 2022, *MNRAS*, 516, 4862
- Javanmardi, B. & Kroupa, P. 2017, *A&A*, 597, A120
- Javanmardi, B., Porciani, C., Kroupa, P., & Pflamm-Altenburg, J. 2015, *ApJ*, 810, 47
- Jia, X. D., Hu, J. P., & Wang, F. Y. 2023, *A&A*, 674, A45
- Jia, X. D., Hu, J. P., Yang, J., Zhang, B. B., & Wang, F. Y. 2022, *MNRAS*, 516, 2575
- Jin, S.-J., Xing, S.-S., Shao, Y., Zhang, J.-F., & Zhang, X. 2023, *Chinese Physics C*, 47, 065104
- Kalbounieh, B., Marinoni, C., & Bel, J. 2023, *Phys. Rev. D*, 107, 023507
- Kalus, B., Schwarz, D. J., Seikel, M., & Wiegand, A. 2013, *A&A*, 553, A56
- Kazantzidis, L. & Perivolaropoulos, L. 2020, *Phys. Rev. D*, 102, 023520
- Keenan, R. C., Barger, A. J., & Cowie, L. L. 2013, *ApJ*, 775, 62
- Kelly, P. L., Rodney, S., Treu, T., et al. 2023, *arXiv e-prints*, arXiv:2305.06367
- Kelly, P. L., Rodney, S. A., Treu, T., et al. 2015, *Science*, 347, 1123
- Kenworthy, W. D., Scolnic, D., & Riess, A. 2019, *ApJ*, 875, 145
- Khadka, N. & Ratra, B. 2020, *MNRAS*, 492, 4456
- Khadka, N., Zajaček, M., Panda, S., Martínez-Aldama, M. L., & Ratra, B. 2022, *MNRAS*, 515, 3729
- Khadka, N., Zajaček, M., Prince, R., et al. 2023, *MNRAS*, 522, 1247
- King, J. A., Webb, J. K., Murphy, M. T., et al. 2012, *MNRAS*, 422, 3370
- Koivisto, T. & Mota, D. F. 2008, *J. Cosmology Astropart. Phys.*, 2008, 018
- Koksbang, S. M. 2021, *Phys. Rev. Lett.*, 126, 231101
- Kolodzig, A., Gilfanov, M., Sunyaev, R., Sazonov, S., & Brusa, M. 2013, *A&A*, 558, A89
- Krishnan, C., Colgáin, E. Ó., Ruchika, Sen, A. A., Sheikh-Jabbari, M. M., & Yang, T. 2020, *Phys. Rev. D*, 102, 103525
- Krishnan, C., Mohayaee, R., Colgáin, E. Ó., Sheikh-Jabbari, M. M., & Yin, L. 2021a, *Classical and Quantum Gravity*, 38, 184001
- Krishnan, C., Mohayaee, R., Colgáin, E. Ó., Sheikh-Jabbari, M. M., & Yin, L. 2022, *Phys. Rev. D*, 105, 063514
- Krishnan, C., Ó Colgáin, E., Sheikh-Jabbari, M. M., & Yang, T. 2021b, *Phys. Rev. D*, 103, 103509
- Kumar Aluri, P., Cea, P., Chingangbam, P., et al. 2023, *Classical and Quantum Gravity*, 40, 094001
- Law, C. J., Bower, G. C., Burke-Spolaor, S., et al. 2018, *ApJS*, 236, 8
- Leung, C., Mena-Parra, J., Masui, K., et al. 2021, *AJ*, 161, 81
- Lewis, A. 2019, *arXiv e-prints*, arXiv:1910.13970
- Li, S.-Y., Li, Y.-L., Zhang, T., et al. 2023a, *Science China Physics, Mechanics, and Astronomy*, 66, 229511
- Li, X. & Lin, H.-N. 2017, *Chinese Physics C*, 41, 065102



- Li, Z., Zhang, B., & Liang, N. 2023b, *MNRAS*, 521, 4406
- Liang, N., Li, Z., Xie, X., & Wu, P. 2022, *ApJ*, 941, 84
- LIGO Scientific Collaboration, Aasi, J., Abbott, B. P., et al. 2015, *Classical and Quantum Gravity*, 32, 074001
- Lin, H.-N., Li, X., & Chang, Z. 2016a, *MNRAS*, 460, 617
- Lin, H.-N., Wang, S., Chang, Z., & Li, X. 2016b, *MNRAS*, 456, 1881
- Liu, T., Yang, X., Zhang, Z., Wang, J., & Biesiada, M. 2023a, *Physics Letters B*, 845, 138166
- Liu, Y., Chen, F., Liang, N., et al. 2022a, *ApJ*, 931, 50
- Liu, Y., Liang, N., Xie, X., et al. 2022b, *ApJ*, 935, 7
- Liu, Y., Yu, H., & Wu, P. 2023b, *ApJ*, 946, L49
- Luković, V. V., Haridasu, B. S., & Vittorio, N. 2020, *MNRAS*, 491, 2075
- Luongo, O., Muccino, M., Colgáin, E. Ó., Sheikh-Jabbari, M. M., & Yin, L. 2022, *Phys. Rev. D*, 105, 103510
- Lusso, E. 2020, *Frontiers in Astronomy and Space Sciences*, 7, 8
- Lusso, E. & Risaliti, G. 2016, *ApJ*, 819, 154
- Lusso, E. & Risaliti, G. 2017, *A&A*, 602, A79
- Malekjani, M., Mc Conville, R., Colgáin, E. Ó., Pourojaghi, S., & Sheikh-Jabbari, M. M. 2023, arXiv e-prints, arXiv:2301.12725
- Mandal, S., Duffell, P. C., Polin, A., & Milisavljevic, D. 2023, arXiv e-prints, arXiv:2305.17324
- Mariano, A. & Perivolaropoulos, L. 2012, *Phys. Rev. D*, 86, 083517
- McConville, R. & Colgáin, E. Ó. 2023, arXiv e-prints, arXiv:2304.02718
- Merloni, A., Predehl, P., Becker, W., et al. 2012, arXiv e-prints, arXiv:1209.3114
- Miao, H., Gong, Y., Chen, X., et al. 2023, *MNRAS*, 519, 1132
- Migkas, K., Pacaud, F., Schellenberger, G., et al. 2021, *A&A*, 649, A151
- Migkas, K., Schellenberger, G., Reiprich, T. H., et al. 2020, *A&A*, 636, A15
- Milaković, D., Lee, C.-C., Molaro, P., & Webb, J. K. 2022, arXiv e-prints, arXiv:2212.02458
- Millon, M., Galan, A., Courbin, F., et al. 2020, *A&A*, 639, A101
- Motoa-Manzano, J., Orjuela-Quintana, J. B., Pereira, T. S., & Valenzuela-Toledo, C. A. 2021, *Physics of the Dark Universe*, 32, 100806
- Ó Colgáin, E., Sheikh-Jabbari, M. M., & Solomon, R. 2023, *Physics of the Dark Universe*, 40, 101216
- Ó Colgáin, E., Sheikh-Jabbari, M. M., Solomon, R., et al. 2022, *Phys. Rev. D*, 106, L041301
- Pastén, E. & Cárdenas, V. H. 2023, *Physics of the Dark Universe*, 40, 101224
- Pavel, K., Gjergo, E., Asencio, E., et al. 2023, *The many tensions with dark-matter based models and implications on the nature of the Universe*
- Pedregosa, F., Varoquaux, G., Gramfort, A., et al. 2011, *Journal of Machine Learning Research*, 12, 2825
- Pelgrims, V. & Hutsemékers, D. 2016, *A&A*, 590, A53
- Perivolaropoulos, L. 2023, *Phys. Rev. D*, 108, 063509
- Perivolaropoulos, L. & Skara, F. 2021, *Phys. Rev. D*, 104, 123511
- Perivolaropoulos, L. & Skara, F. 2022, *New A Rev.*, 95, 101659
- Perivolaropoulos, L. & Skara, F. 2023, *MNRAS*, 520, 5110
- Planck Collaboration, Adam, R., Ade, P. A. R., et al. 2016, *A&A*, 594, A1
- Planck Collaboration, Aghanim, N., Akrami, Y., et al. 2020a, *A&A*, 641, A1
- Planck Collaboration, Aghanim, N., Akrami, Y., et al. 2020b, *A&A*, 641, A6
- Planck Collaboration, Akrami, Y., Ashdown, M., et al. 2020c, *A&A*, 641, A7
- Porredon, A., Crocce, M., Elvin-Poole, J., et al. 2022, *Phys. Rev. D*, 106, 103530
- Predehl, P. 2012, in *Society of Photo-Optical Instrumentation Engineers (SPIE) Conference Series*, Vol. 8443, *Space Telescopes and Instrumentation 2012: Ultraviolet to Gamma Ray*, ed. T. Takahashi, S. S. Murray, & J.-W. A. den Herder, 84431R
- Rahman, W., Trotta, R., Boruah, S. S., Hudson, M. J., & van Dyk, D. A. 2022, *MNRAS*, 514, 139
- Rameez, M., Mohayaee, R., Sarkar, S., & Colin, J. 2018, *MNRAS*, 477, 1772
- Refsdal, S. 1964, *MNRAS*, 128, 295
- Riess, A. G. 2020, *Nature Reviews Physics*, 2, 10
- Riess, A. G. & Breuval, L. 2023, arXiv e-prints, arXiv:2308.10954
- Riess, A. G., Casertano, S., Yuan, W., Macri, L. M., & Scolnic, D. 2019, *ApJ*, 876, 85
- Riess, A. G., Yuan, W., Macri, L. M., et al. 2022, *ApJ*, 934, L7
- Risaliti, G. & Lusso, E. 2019, *Nature Astronomy*, 3, 272
- Rubart, M., Bacon, D., & Schwarz, D. J. 2014, *A&A*, 565, A111
- Sakr, Z. 2023, arXiv e-prints, arXiv:2305.02846
- Sanidas, S., Caleb, M., Driessen, L., et al. 2018, in *Pulsar Astrophysics the Next Fifty Years*, ed. P. Weltevrede, B. B. P. Perera, L. L. Preston, & S. Sanidas, Vol. 337, 406–407
- Schwarz, D. J. & Weinhorst, B. 2007, *A&A*, 474, 717
- Scolnic, D., Brout, D., Carr, A., et al. 2022, *ApJ*, 938, 113
- Scolnic, D. M., Jones, D. O., Rest, A., et al. 2018, *ApJ*, 859, 101
- Secrest, N. J., von Hausegger, S., Rameez, M., et al. 2021, *ApJ*, 908, L51
- Shah, P., Lemos, P., & Lahav, O. 2021, *A&A Rev.*, 29, 9
- Shim, J., Park, C., Kim, J., & Hong, S. E. 2023, arXiv e-prints, arXiv:2305.09888
- Singal, A. K. 2019, *Phys. Rev. D*, 100, 063501
- Singal, A. K. 2023, arXiv e-prints, arXiv:2303.05141
- Smith, M., D'Andrea, C. B., Sullivan, M., et al. 2020, *AJ*, 160, 267
- Stahl, B. E., Zheng, W., de Jaeger, T., et al. 2019, *MNRAS*, 490, 3882
- Sun, Z. Q. & Wang, F. Y. 2018, *MNRAS*, 478, 5153
- Sun, Z. Q. & Wang, F. Y. 2019, *European Physical Journal C*, 79, 783
- Tang, L., Lin, H.-N., Liu, L., & Li, X. 2023, arXiv e-prints, arXiv:2309.11320
- Tegmark, M., de Oliveira-Costa, A., & Hamilton, A. J. 2003, *Phys. Rev. D*, 68, 123523
- Tiwari, P. & Jain, P. 2019, *A&A*, 622, A113
- Tripp, R. 1998, *A&A*, 331, 815
- Turnbull, S. J., Hudson, M. J., Feldman, H. A., et al. 2012, *MNRAS*, 420, 447
- Vagnozzi, S. 2023, *Universe*, 9, 393
- Van Raamsdonk, M. & Waddell, C. 2023, arXiv e-prints, arXiv:2305.04946
- Verde, L., Treu, T., & Riess, A. G. 2019, *Nature Astronomy*, 3, 891
- Wang, D. 2022, *Phys. Rev. D*, 106, 063515
- Wang, F. Y. & Dai, Z. G. 2013, *MNRAS*, 432, 3025
- Wang, F. Y., Dai, Z. G., & Liang, E. W. 2015, *New A Rev.*, 67, 1
- Wang, F. Y., Hu, J. P., Zhang, G. Q., & Dai, Z. G. 2022, *ApJ*, 924, 97
- Wang, J. S. & Wang, F. Y. 2014, *MNRAS*, 443, 1680
- Wang, K. & Chen, K.-P. 2023, arXiv e-prints, arXiv:2304.13945
- Wang, Y.-Y., Tang, S.-P., Jin, Z.-P., & Fan, Y.-Z. 2023, *ApJ*, 943, 13
- Wang, Y.-Y. & Wang, F. Y. 2018, *MNRAS*, 474, 3516
- Watkins, R., Allen, T., Bradford, C. J., et al. 2023, arXiv e-prints, arXiv:2302.02028
- Webb, J. K., King, J. A., Murphy, M. T., et al. 2011, *Phys. Rev. Lett.*, 107, 191101
- Wei, J., Cordier, B., Antier, S., et al. 2016, arXiv e-prints, arXiv:1610.06892
- Wong, K. C., Suyu, S. H., Chen, G. C. F., et al. 2020, *MNRAS*, 498, 1420
- Wu, Q., Zhang, G.-Q., & Wang, F.-Y. 2022, *MNRAS*, 515, L1
- Xu, Y.-T., Dai, J.-P., Zhao, D., & Xia, J.-Q. 2022, *MNRAS*, 515, 5587
- Yang, X., Wang, F. Y., & Chu, Z. 2014, *MNRAS*, 437, 1840
- Yuan, W., Zhang, C., Feng, H., et al. 2015, arXiv e-prints, arXiv:1506.07735
- Zajack, M., Czerny, B., Khadka, N., et al. 2023, arXiv e-prints, arXiv:2305.08179
- Zhao, D. & Xia, J.-Q. 2021a, *European Physical Journal C*, 81, 948
- Zhao, D. & Xia, J.-Q. 2021b, *European Physical Journal C*, 81, 694
- Zhao, D. & Xia, J.-Q. 2022, *MNRAS*, 511, 5661
- Zhao, D., Zhou, Y., & Chang, Z. 2019, *MNRAS*, 486, 5679
- Zhao, Z.-W., Zhang, J.-G., Li, Y., et al. 2022, arXiv e-prints, arXiv:2212.13433
- Zhou, Y., Zhao, Z.-C., & Chang, Z. 2017, *ApJ*, 847, 86

## Appendix A: Attached materials

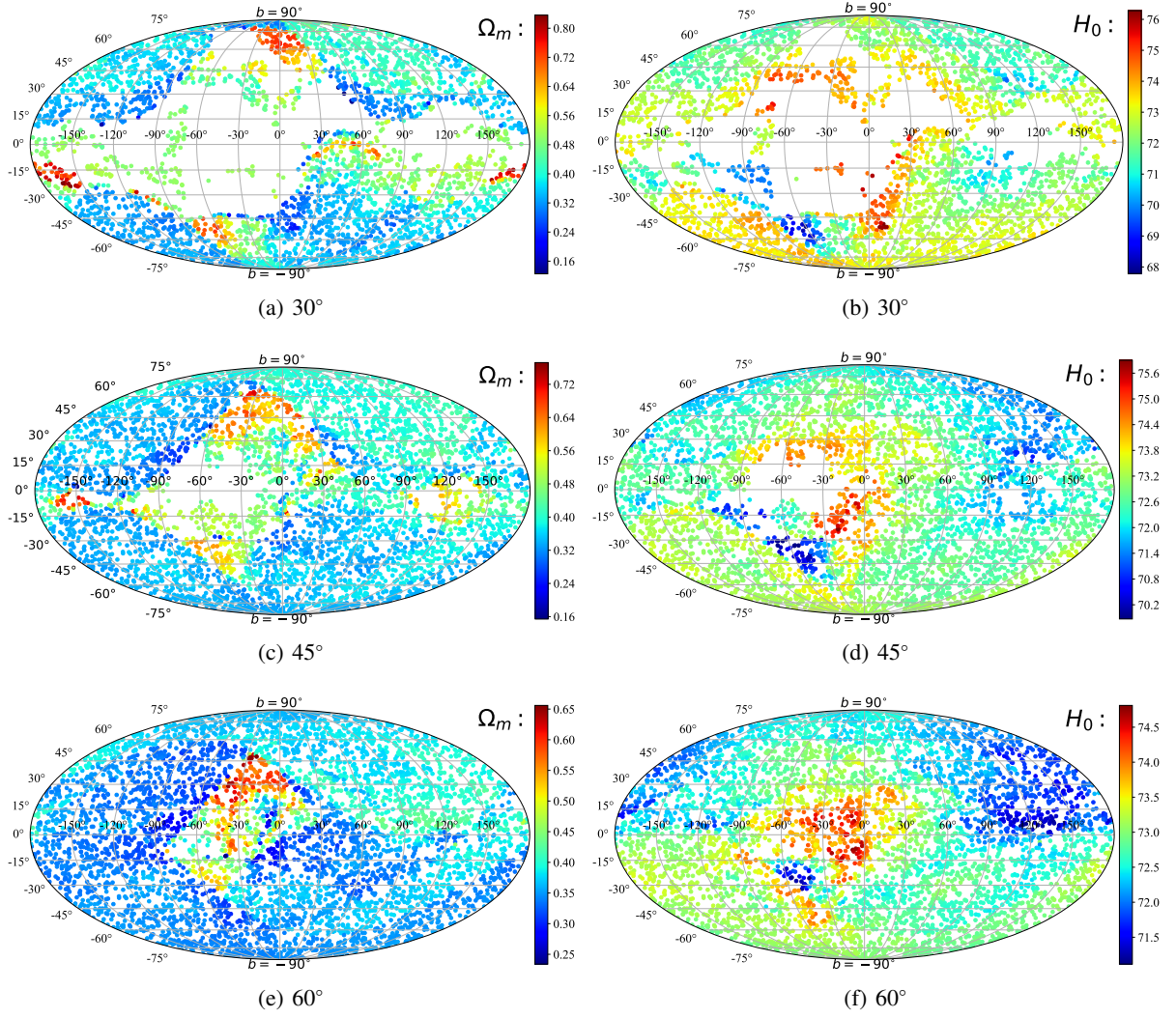


**Fig. A.1.** All-sky distribution of the cosmological parameter ( $\Omega_m$  and  $H_0$ ) utilizing the Pantheon+ sample combined with the RF method with different screening angles including 30°, 45° and 60°. Panels (a) and (b) show the results using the hemisphere method with 30°. Panels (c) and (d) are the results of 45°. Panels (e) and (f) are the results of 60°. The proportions of the wrong fitting results are 30.34%, 6.47% and 0.70% for the screening angles 30°, 45° and 60°, respectively.

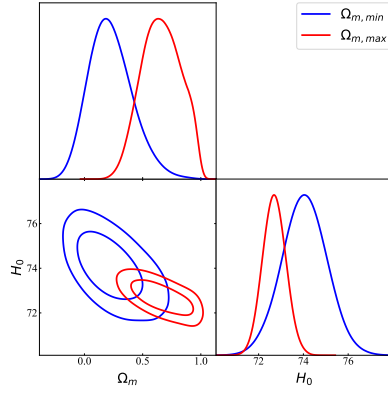


**Fig. A.2.** Confidence contours ( $1\sigma$  and  $2\sigma$ ) and marginalized likelihood distributions for the parameters space ( $\Omega_m$  and  $H_0$ ) in the spatially flat  $\Lambda$ CDM model from SNe Ia subsamples which corresponds to  $\Omega_{m,min}$  and  $\Omega_{m,max}$ . The best fits are  $\Omega_{m,min} = 0.23^{+0.20}_{-0.17}$  and  $H_0 = 74.05^{+1.00}_{-1.00}$  km s $^{-1}$  Mpc $^{-1}$  and  $\Omega_{m,max} = 0.66^{+0.17}_{-0.17}$  and  $H_0 = 72.70^{+0.52}_{-0.52}$  km s $^{-1}$  Mpc $^{-1}$ .